

FIGURE 1.1 SAR imaging geometry in strip-map mode.

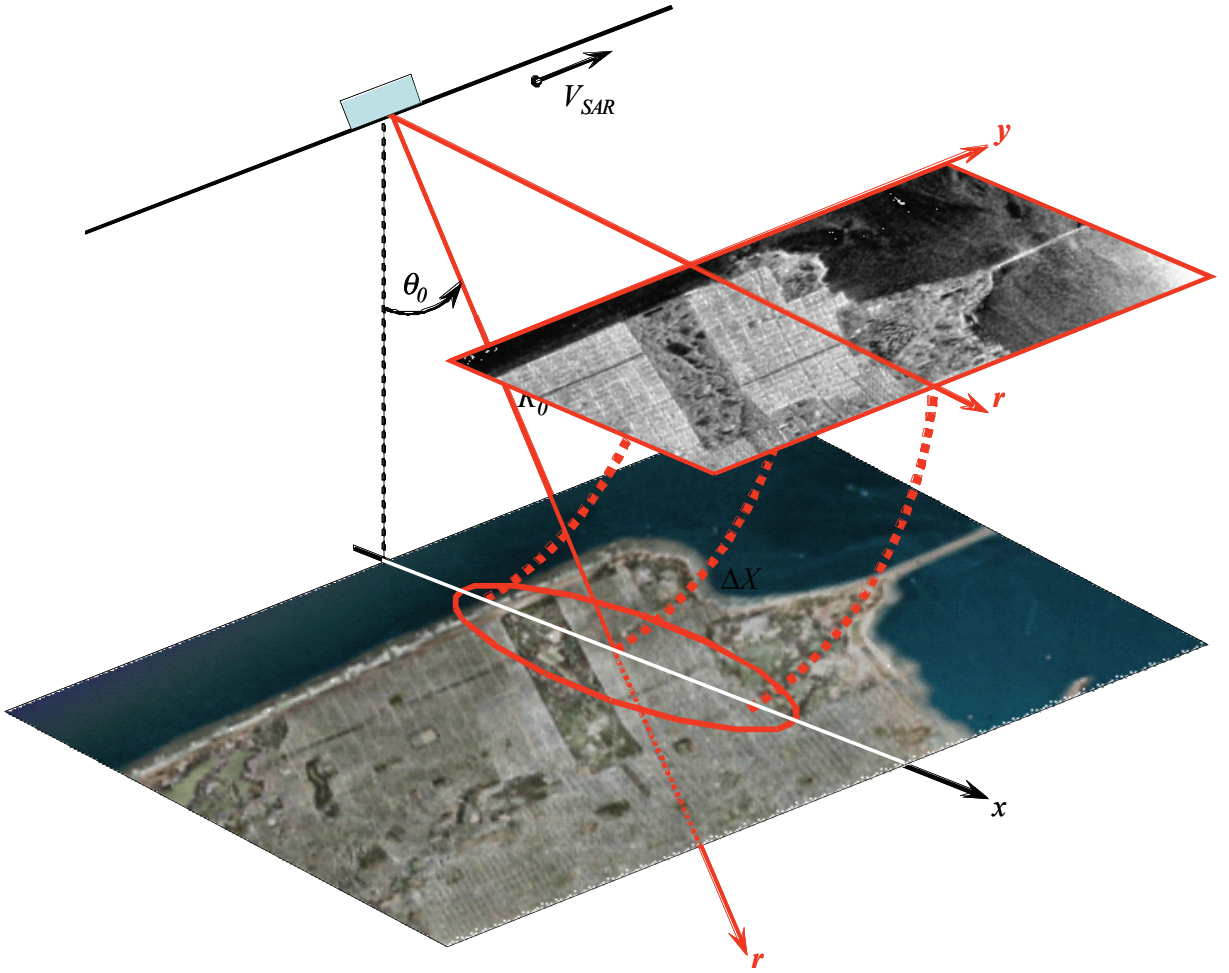


FIGURE 1.4 Ground range to slant range projection.

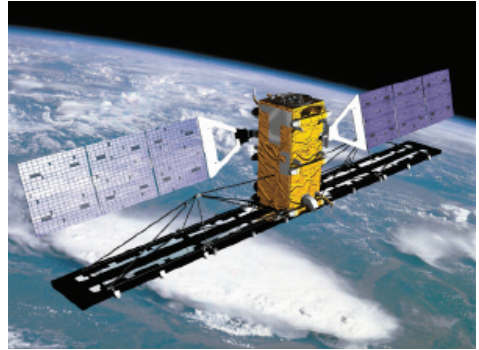


Pod under the right wing and cutaway view of the SETHI pod (L and X antennas)

FIGURE 1.9 Polarimetric SETHI airborne sensors (ONERA-DEMRA). (Courtesy of ONERA and Dr. J.M. Boutry.)



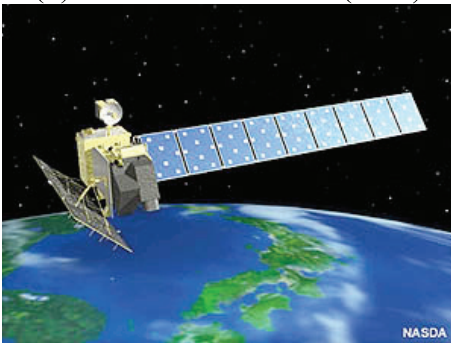
(a) SIR-C / X SAR (NASA / DARA / ASI)



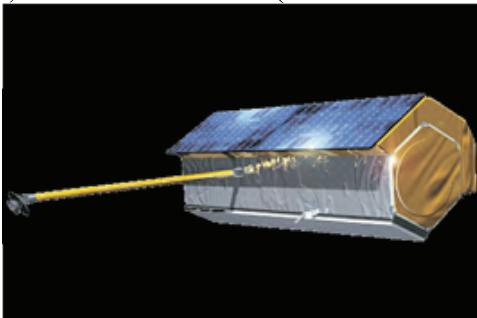
(e) RADARSAT-2 (CSA / MDA)



(b) ENVISAT – ASAR (ESA)



(c) ALOS – PALSAR (JAXA / JAROS)



(d) TerraSAR-X (BMBF / DLR / Astrium GmbH)

FIGURE 1.10 Polarimetric space-borne sensors. (a) SIR-C = X SAR (NASA = DARA = ASI), (b) ENVISAT-ASAR (ESA), (c) ALOS-PALSAR (JAXA = JAROS), (d) TerraSAR-X (BMBF = DLR = Astrium GmbH), (e) RADARSAT-2 (CSA = MDA). (Courtesy of ESA [19,42], NASA[41], JAXA[43,44], DLR[45,46], CSA[47,48].)

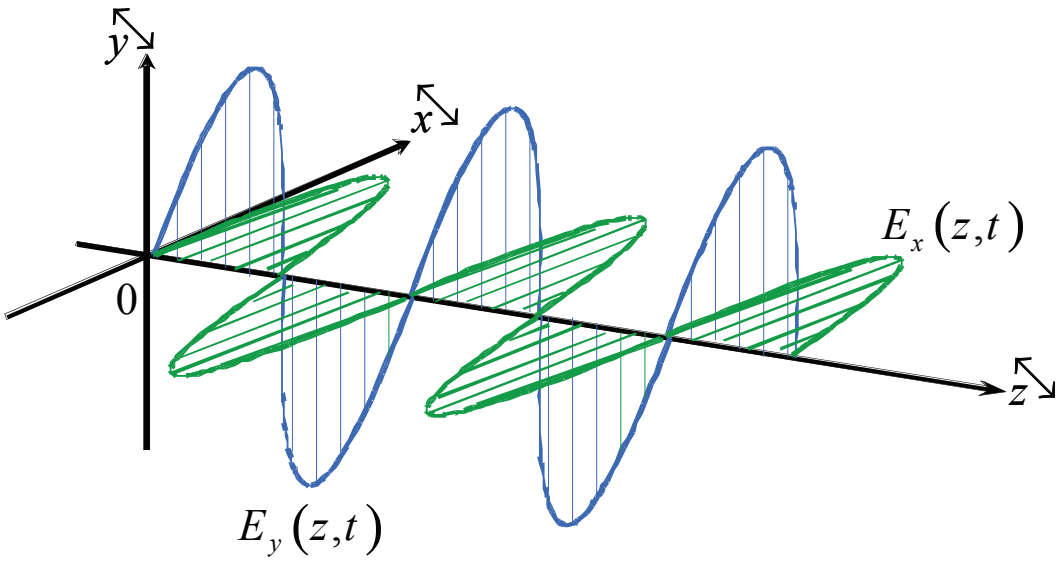


FIGURE 2.1 Spatial evolution of monochromatic plane wave components.

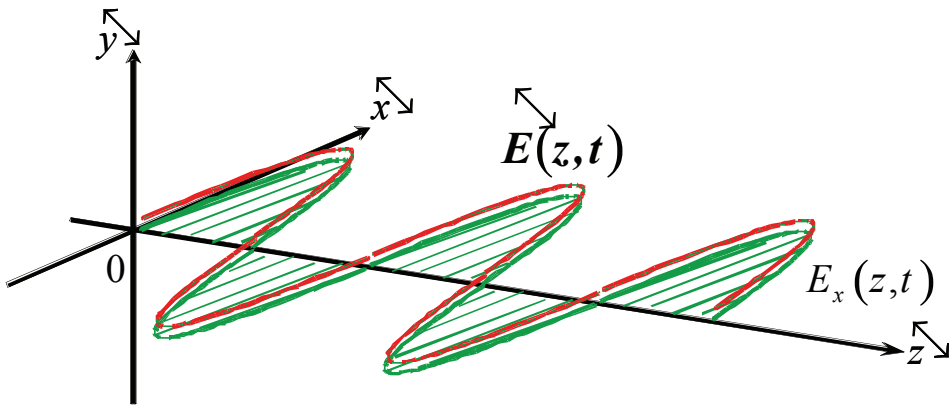


FIGURE 2.2 Spatial evolution of a linearly (horizontal) polarized plane wave.

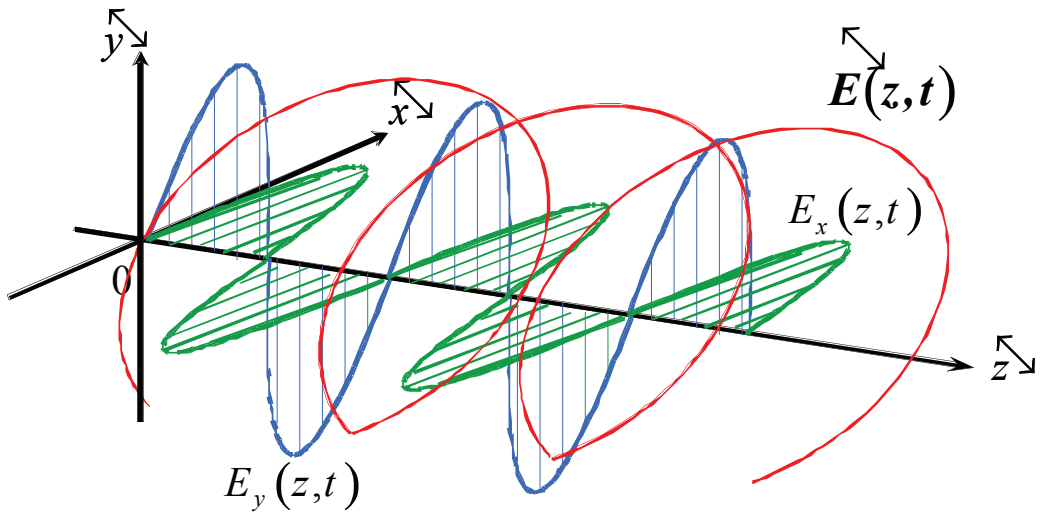


FIGURE 2.3 Spatial evolution of a circularly polarized plane wave.

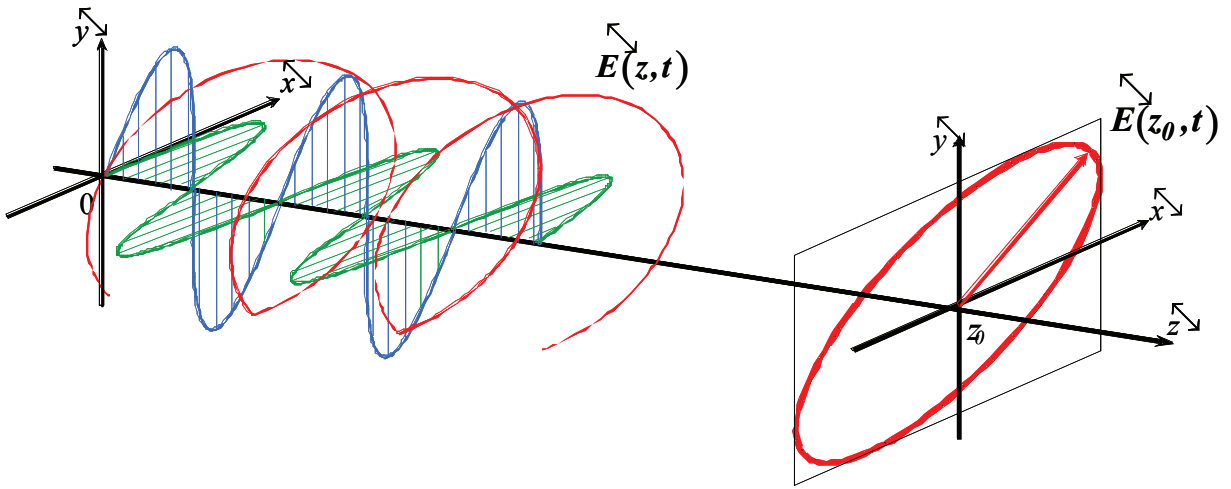


FIGURE 2.4 Temporal trajectory of a monochromatic plane wave at a fixed abscissa $z = z_0$.



(a) (\hat{h}, \hat{v}) basis

$$\text{Blue} = S_{HH} + S_{VV},$$

$$\text{Red} = S_{HH} - S_{VV}$$

$$\text{Green} = 2S_{HV}$$

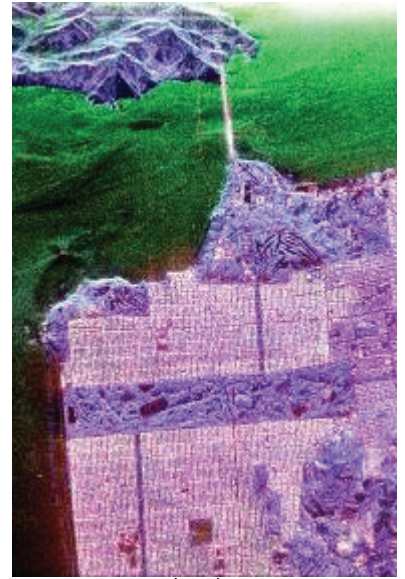


(b) (\hat{a}, \hat{a}_\perp) basis

$$\text{Blue} = S_{AA} + S_{A_\perp A_\perp},$$

$$\text{Red} = S_{AA} - S_{A_\perp A_\perp}$$

$$\text{Green} = 2S_{AA_\perp}$$



(c) (\hat{l}, \hat{l}_\perp) basis

$$\text{Blue} = S_{LL} + S_{L_\perp L_\perp},$$

$$\text{Red} = S_{LL} - S_{L_\perp L_\perp}$$

$$\text{Green} = 2S_{LL_\perp}$$

FIGURE 3.15 Color coded images for different polarization basis.

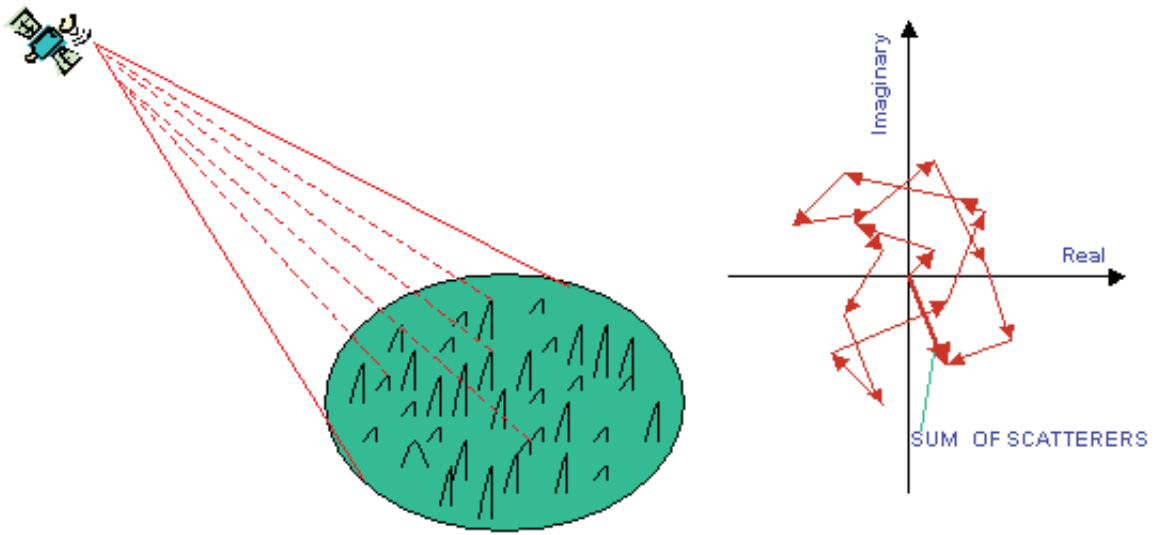


FIGURE 4.1 Speckle formation.

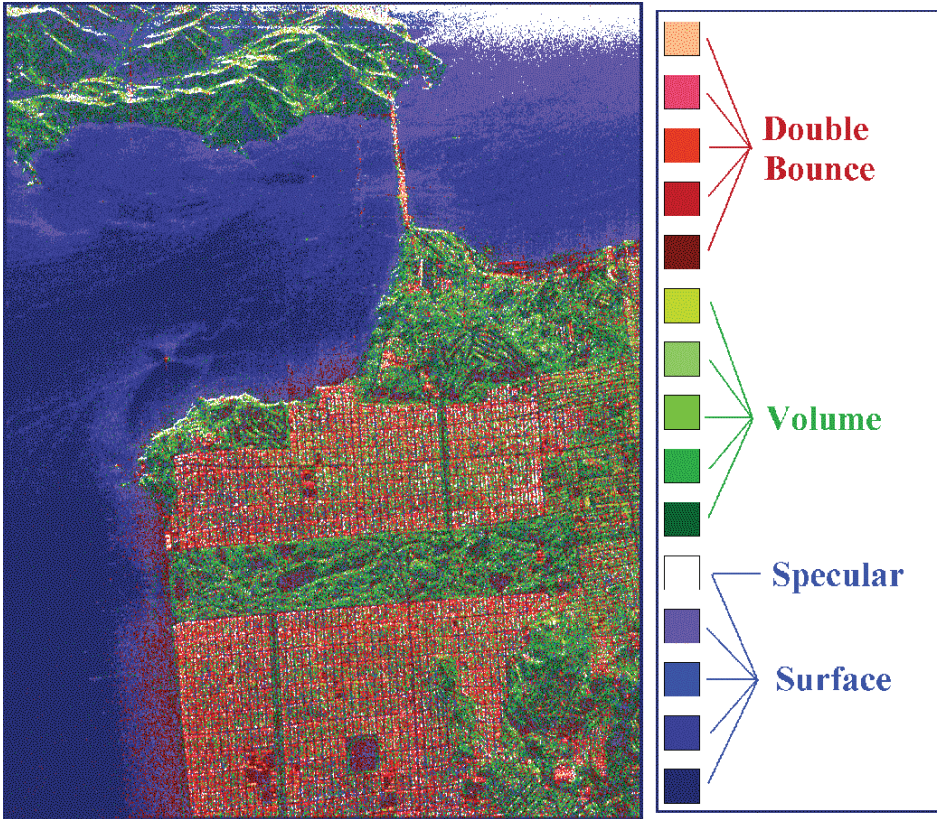
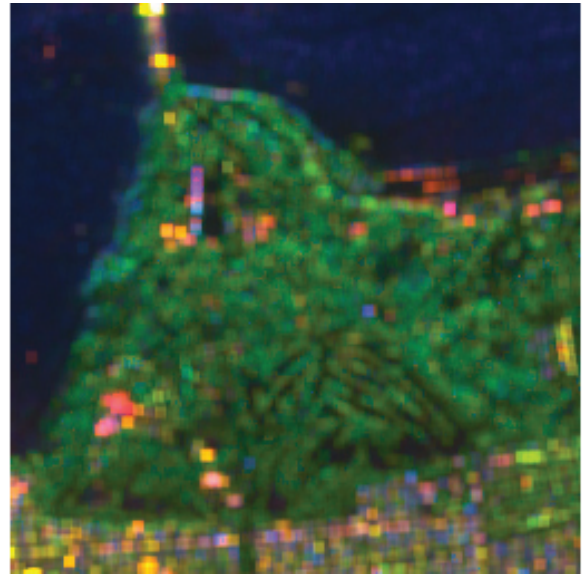


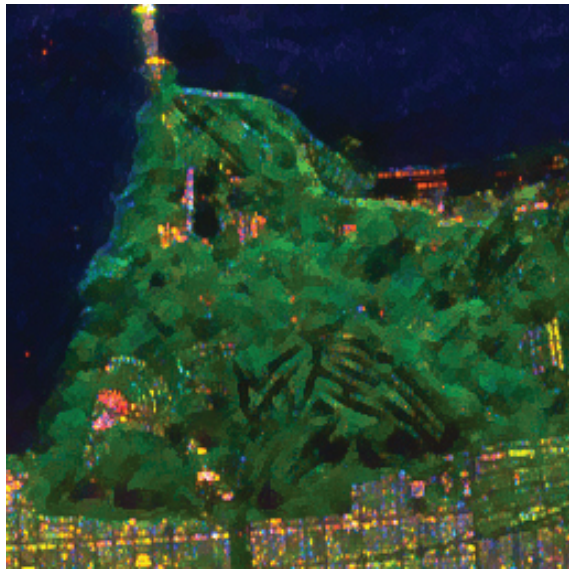
FIGURE 5.11 Unsupervised classification based on scattering properties using the Freeman and Durden decomposition, and the Wishart classifier. The color-coded class label is shown on the right. Speckle filtering is based on this classification map to preserve dominant scattering properties.



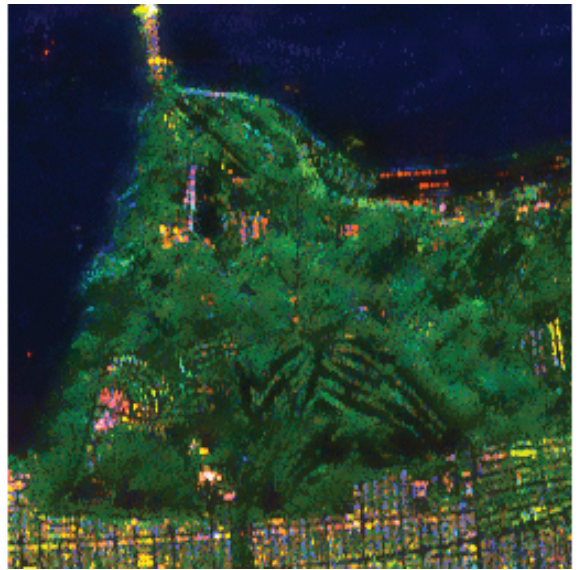
(A) Original image (Freeman/Durden)



(B) 5x5 boxcar filter (Freeman/Durden)



(C) Refined POLSAR filter

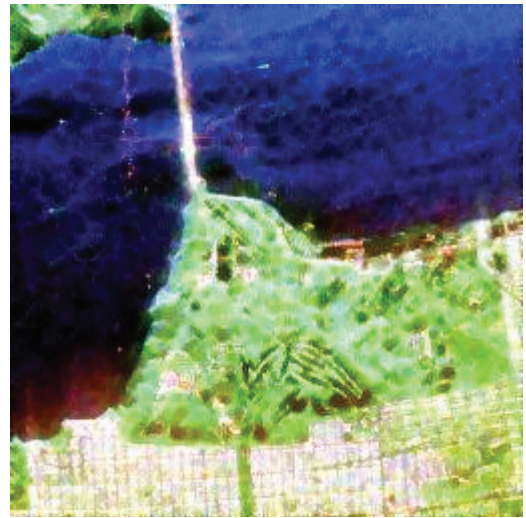


(D) The scattering model

FIGURE 5.14 Comparison of speckle filtering results based on Freeman and Durden decomposition to show their capability to preserve scattering properties. The original is shown in (A). The 5×5 boxcar filter in (B) reveals the overall blurring problem. The refined PolSAR filter (C) and the scattering model-based algorithm (D) are comparable, but the latter retains better resolution.

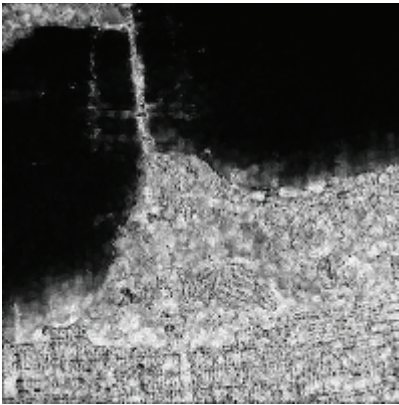


Single Look Image

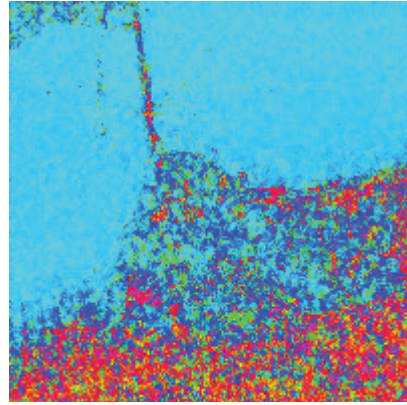


Filtered Image (Lee filter)

Color coded: $Red = T_{22} = \frac{1}{2}|S_{11} - S_{22}|^2$, $Green = T_{33} = 2|S_{12}|^2$, $Blue = T_{11} = \frac{1}{2}|S_{11} + S_{22}|^2$



Modulus



Argument

FIGURE 6.1 Correlation coefficient $\langle s_{11}s_{22}^* \rangle / \sqrt{\langle |s_{11}|^2 \rangle \langle |s_{22}|^2 \rangle}$ after application of a Lee filter.

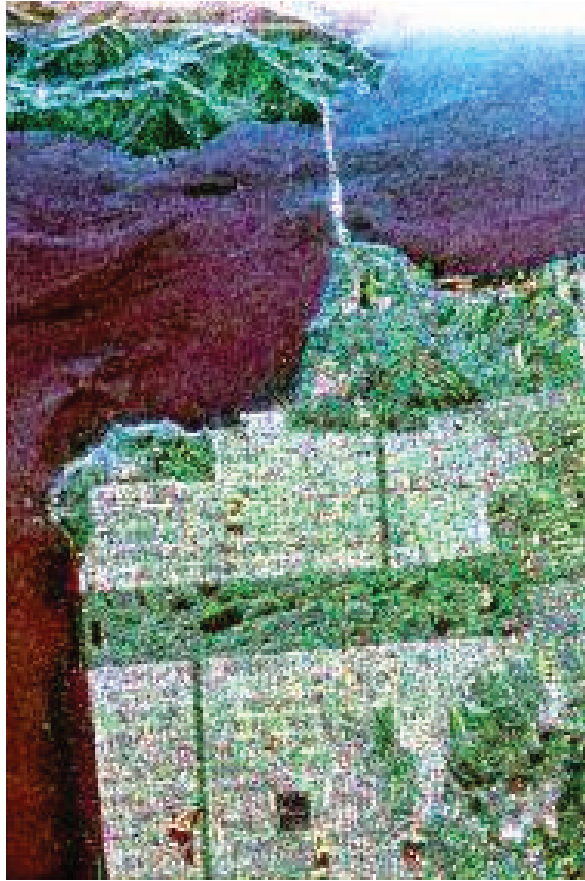


FIGURE 6.4 Color-coded image of the Huynen target decomposition: red, T_{22T} ; green, T_{33T} ; and blue, T_{11T} .



FIGURE 6.6 Color-coded image of the Barnes and Holmes first target decomposition: red, T_{22T} ; green, T_{33T} ; and blue, T_{11T} .



FIGURE 6.8 Color-coded image of the Barnes and Holmes second target decomposition: red, T_{22T} ; green, T_{33T} ; and blue, T_{11T} .



FIGURE 6.10 Color-coded image of the Cloude target decomposition: red, T_{22} ; green, T_{33} ; and blue, T_{11} .



FIGURE 6.12 Color-coded image of the Holmes target decomposition: red, T_{22} ; green, T_{33} ; and blue, I_1 .

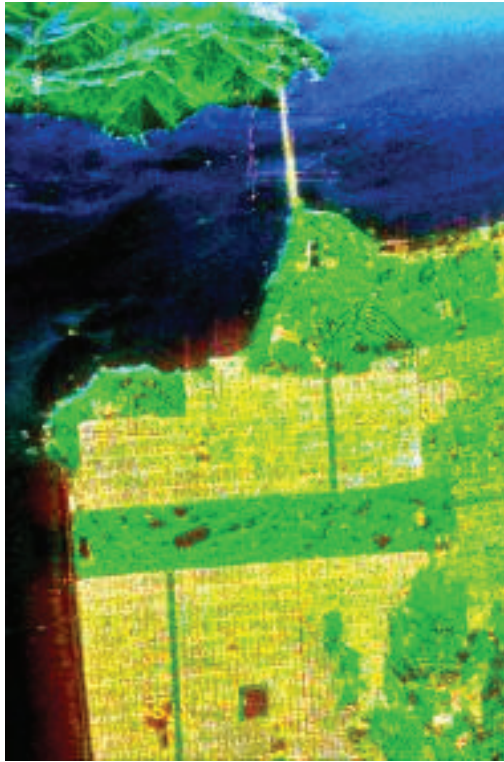


FIGURE 6.14 Color-coded image of the Freeman–Durden target decomposition: red, P_D ; green, P_V ; and blue, P_S .

$10 \log \left(\frac{\langle S_{VV} ^2 \rangle}{\langle S_{HH} ^2 \rangle} \right)$	$-4dB$	$-2dB$	$0dB$	$+2dB$	$+4dB$
$\langle \mathbf{C}_{3V} \rangle_\theta$	$\frac{f_V}{15} \begin{bmatrix} 8 & 0 & 2 \\ 0 & 4 & 0 \\ 2 & 0 & 3 \end{bmatrix}$		$\frac{f_V}{8} \begin{bmatrix} 3 & 0 & 1 \\ 0 & 2 & 0 \\ 1 & 0 & 3 \end{bmatrix}$		$\frac{f_V}{15} \begin{bmatrix} 3 & 0 & 2 \\ 0 & 4 & 0 \\ 2 & 0 & 8 \end{bmatrix}$

FIGURE 6.15: Choice of the volume scattering averaged covariance matrices $\langle \mathbf{C}_{3V} \rangle_\theta$



FIGURE 6.18 Color-coded image of the Yamaguchi target decomposition: red, P_D ; green, P_V ; and blue, P_S .



FIGURE 6.22 Color-coded image of the Pauli decomposition: red, $|b|^2$; green, $|c|^2$; and blue, $|a|^2$.



FIGURE 6.24 Color-coded image of the Krogager decomposition: red, k_D ; green, k_H ; and blue, k_S .

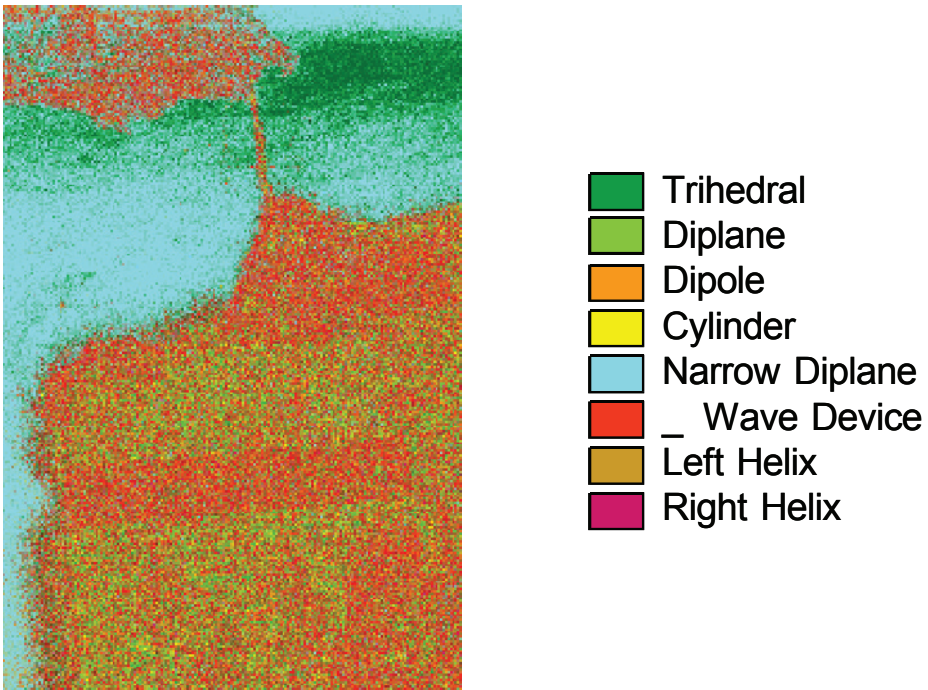


FIGURE 6.27 Cameron coherent scattering matrix classification.



FIGURE 7.2 Pauli color coded mean target image: red, T_{22} , green, T_{33} , blue, T_{11} .

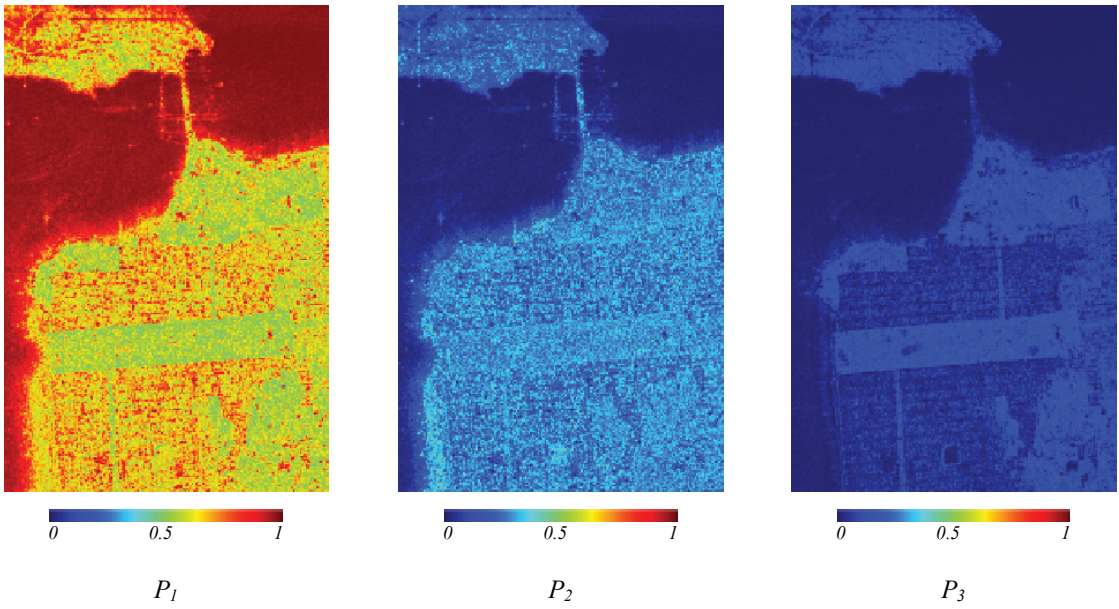


FIGURE 7.3 The three roll-invariant pseudoprobabilities (P_1, P_2, P_3).

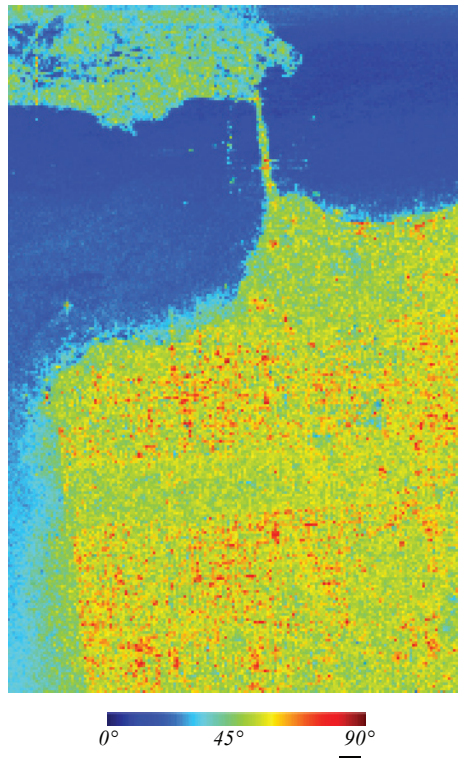


FIGURE 7.4 Roll-invariant $\bar{\alpha}$ parameter.

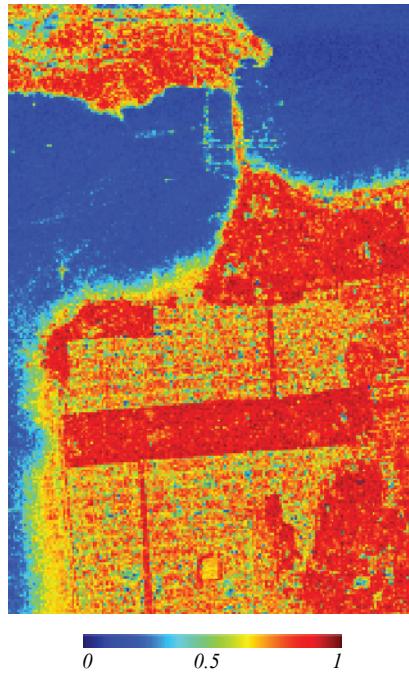


FIGURE 7.5 Roll-invariant entropy H parameter.

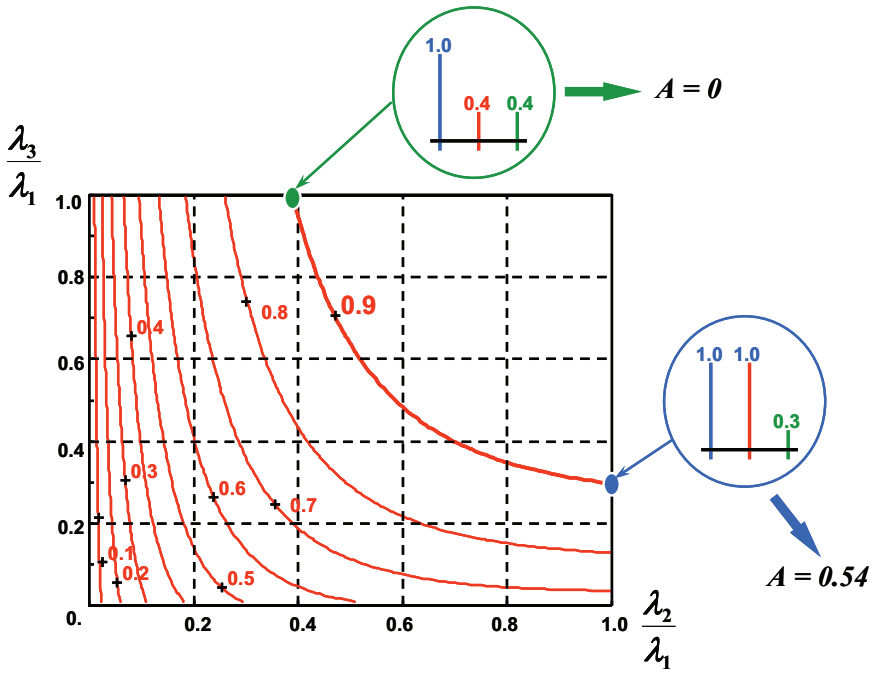


FIGURE 7.6 Variation of the entropy H versus the second and third normalized eigenvalues (λ_2/λ_1) and (λ_3/λ_1).

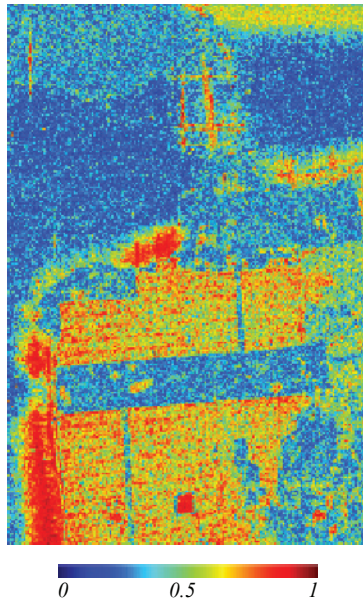


FIGURE 7.7 Roll-invariant anisotropy A parameter.

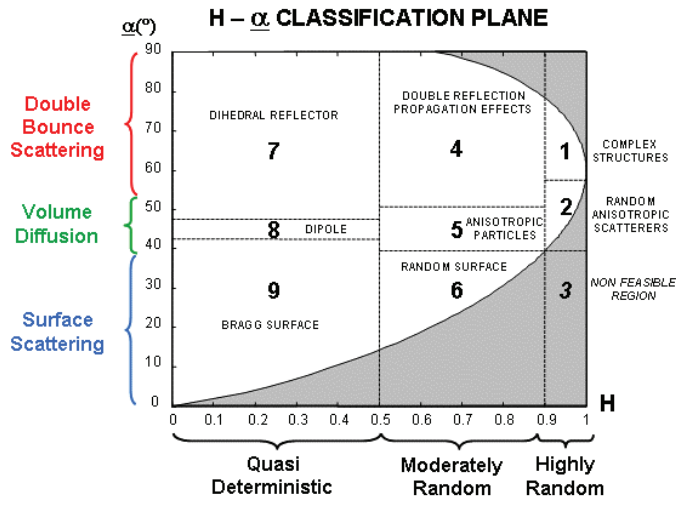


FIGURE 7.8 Two-dimensional $H/\bar{\alpha}$ plane.

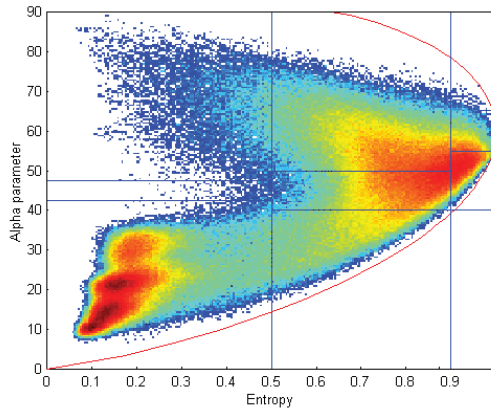


FIGURE 7.9 PolSAR data distribution in the 2-D H/α plane.

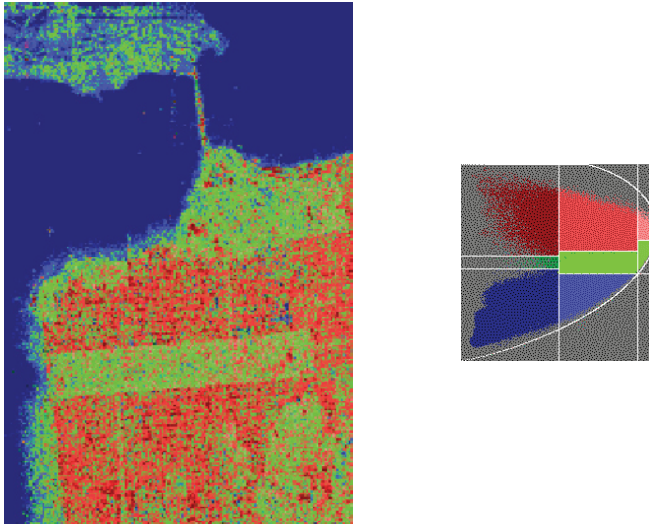


FIGURE 7.10 Unsupervised segmentation of the San Francisco PolSAR image using the 2-D H/α plane.

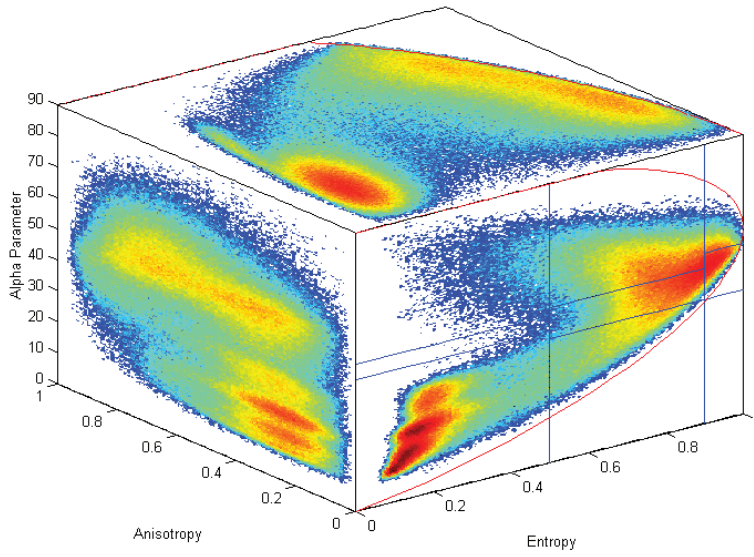


FIGURE 7.11 PolSAR data distribution in the 3-D $H/A/\alpha$ space.

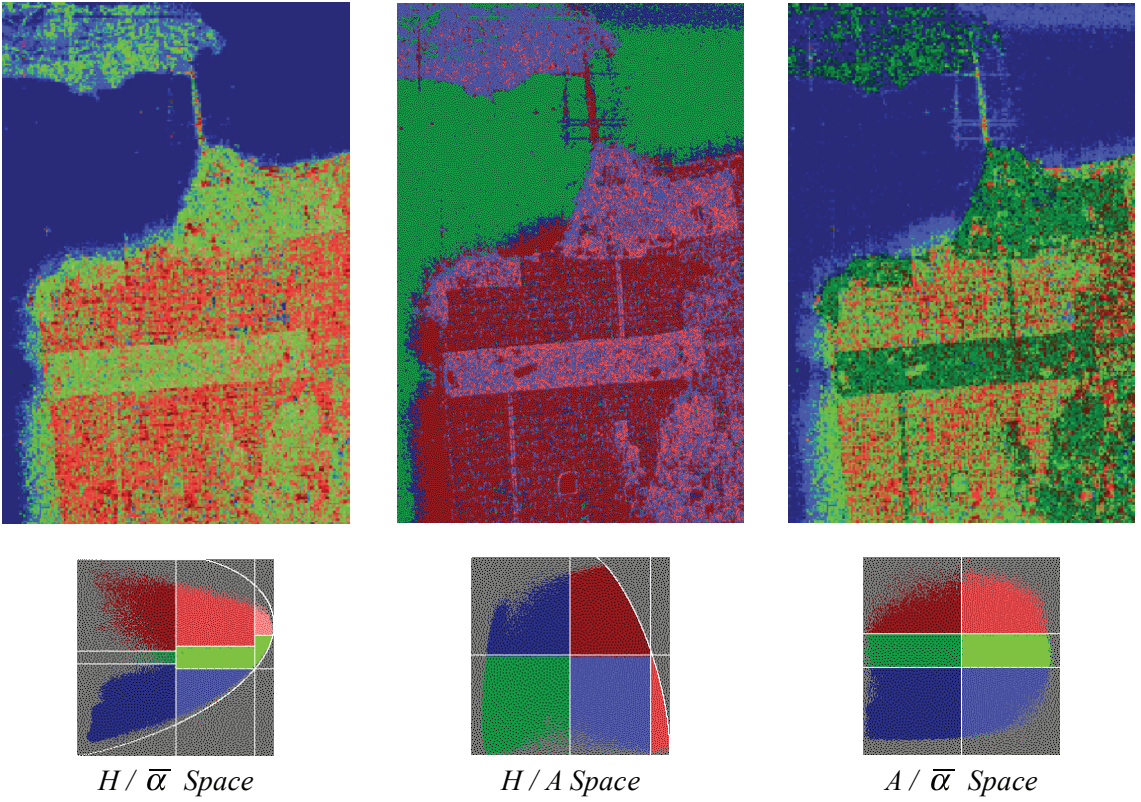


FIGURE 7.12 Unsupervised segmentation of the San Francisco PolSAR image using the 3-D $H/A/\bar{\alpha}$ space.

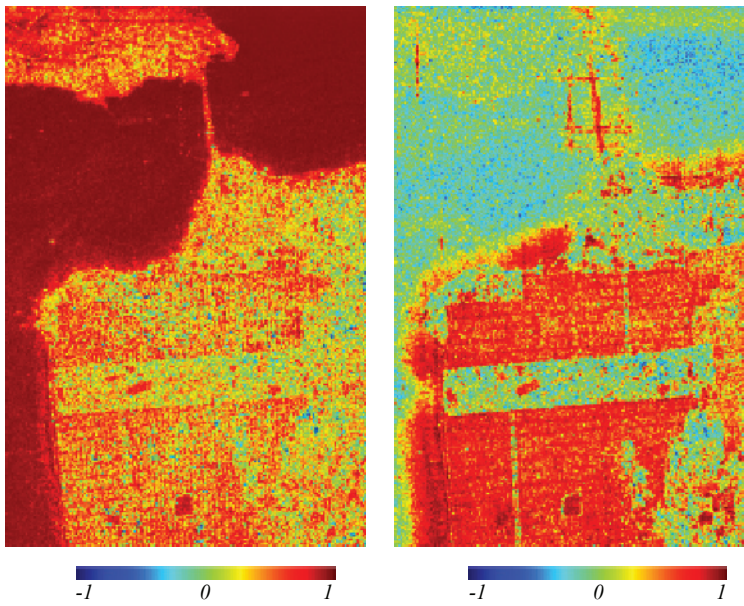


FIGURE 7.15 Single bounce Eigenvalue Relative Difference-SERD (left) and Double bounce Eigenvalue Relative Difference-DERD (right) parameters.

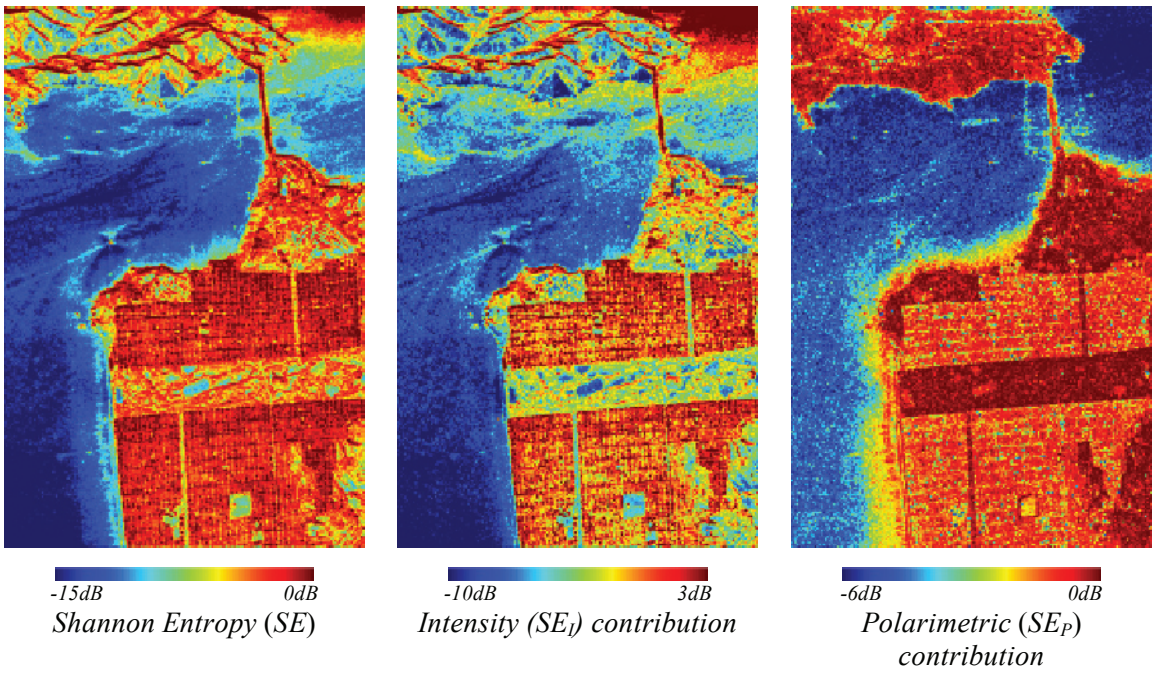


FIGURE 7.16 SE parameter and the two contribution terms.

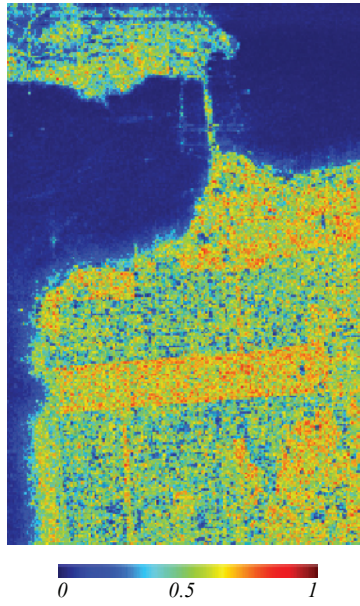


FIGURE 7.17 Roll-invariant p_R parameter.

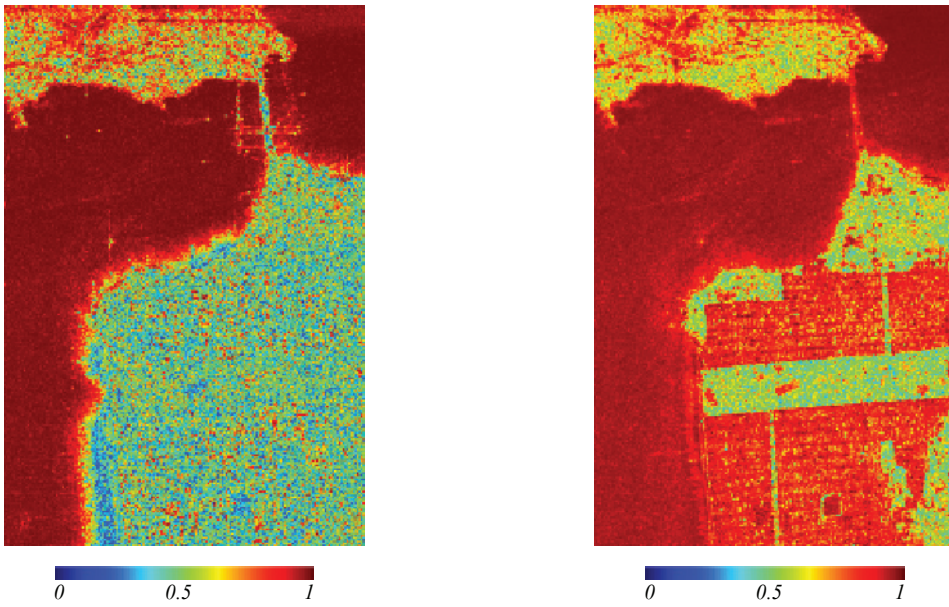


FIGURE 7.18 Roll-invariant PA (left) and PF (right) parameters.

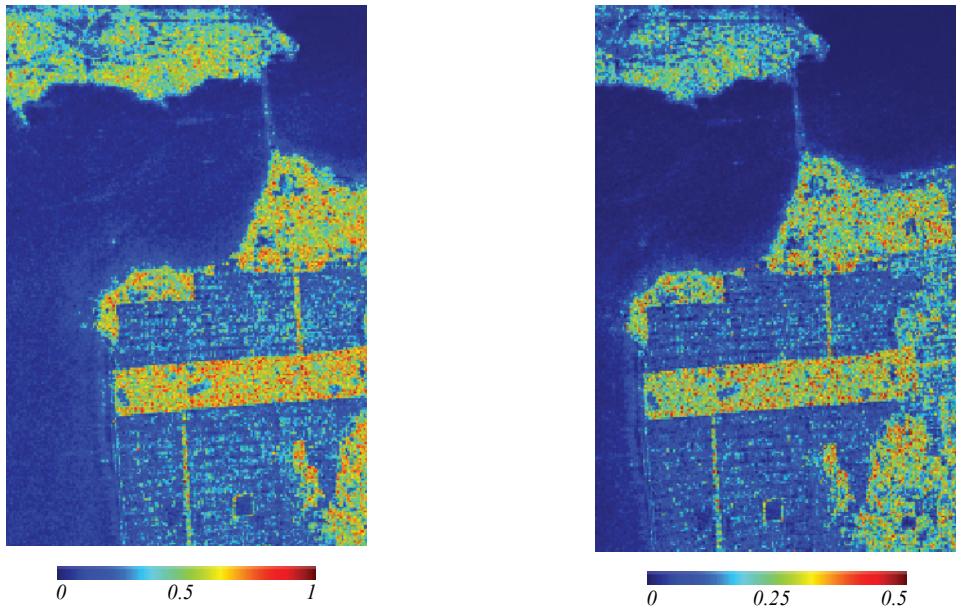
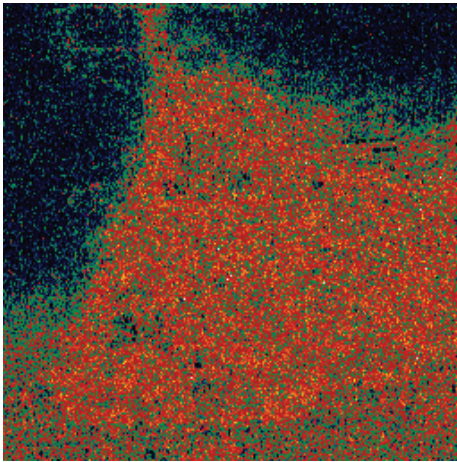
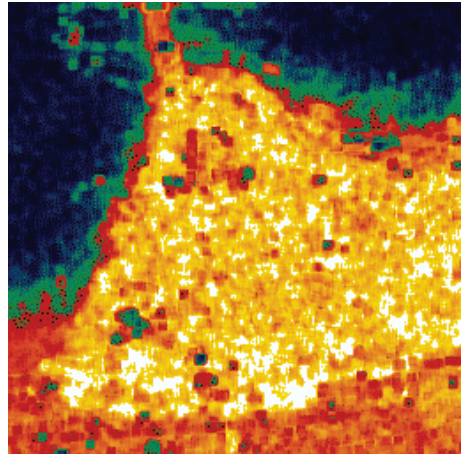


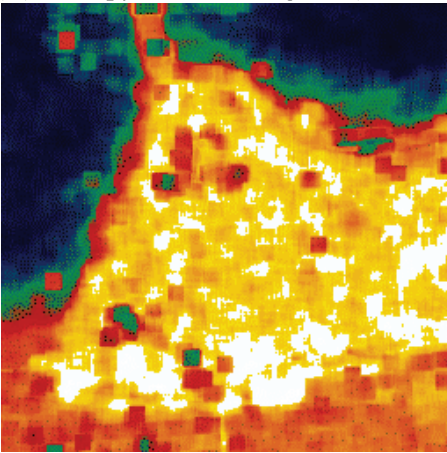
FIGURE 7.19 Roll-invariant RVI (left) and PH (right) parameters.



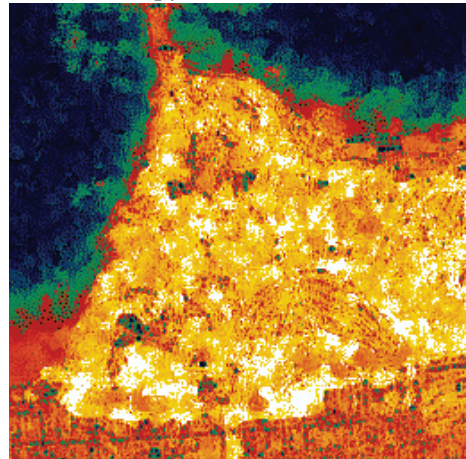
(A) Entropy from the original (4-looks)



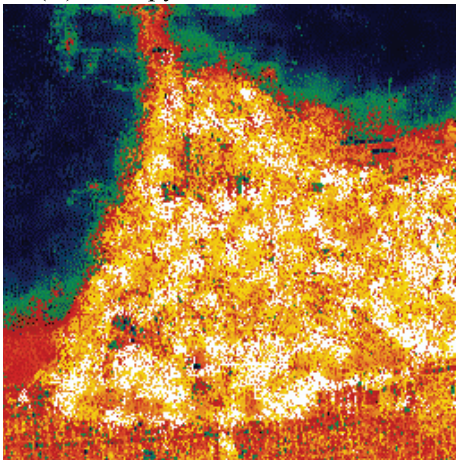
(B) Entropy from the 5×5 boxcar



(C) Entropy from the 9×9 boxcar



(D) Entropy from the refined Lee PolSAR filter

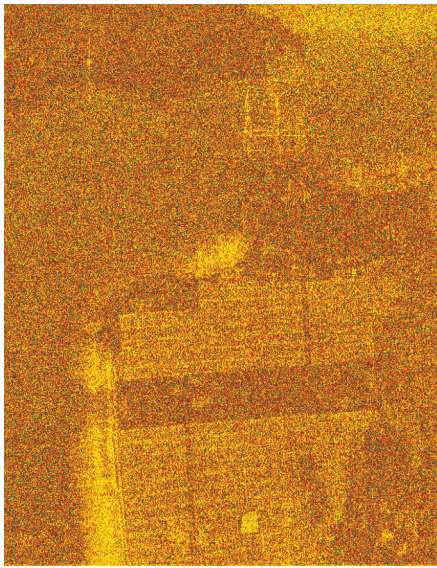


(E) Entropy from the scattering model based filter

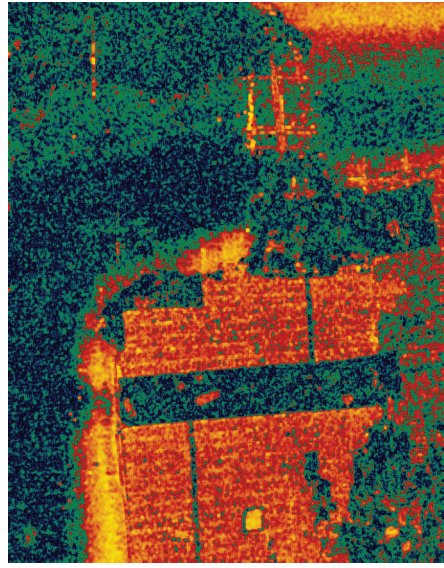


(F) Entropy scale

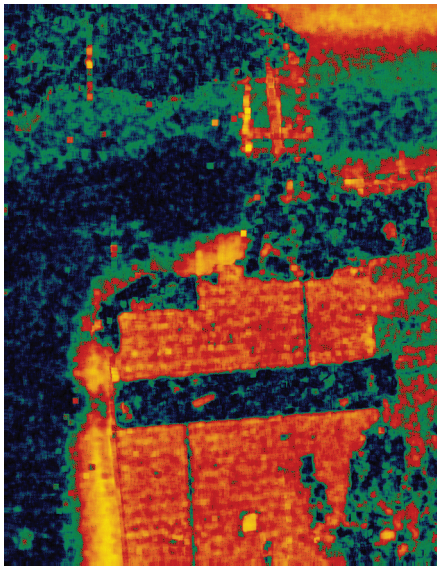
FIGURE 7.20 Speckle filtering effect on the entropy (H) values. (A) entropy from the original (4-looks); (B) entropy from the 5×5 boxcar; (C) entropy from the 9×9 boxcar (D) entropy from the refined Lee PolSAR filter; (E) entropy from the scattering model based filter; and (F) entropy scale.



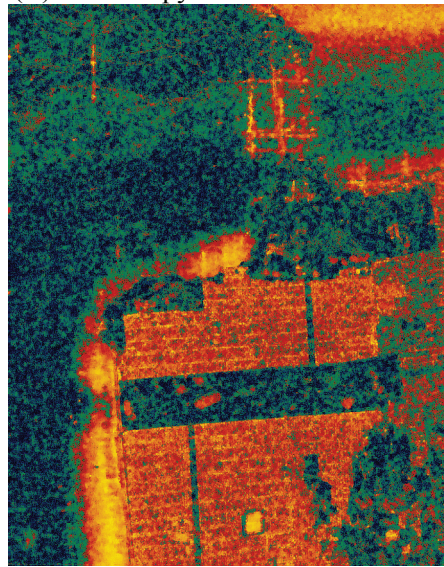
(A) Anisotropy from the original (4-looks)



(B) Anisotropy from the 5x5 boxcar

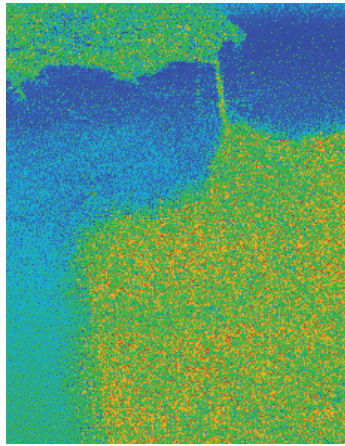


(C) Anisotropy from the 9x9 boxcar

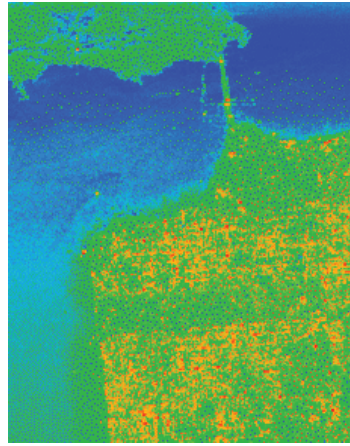


(D) Anisotropy from the refined Lee PolSAR filter

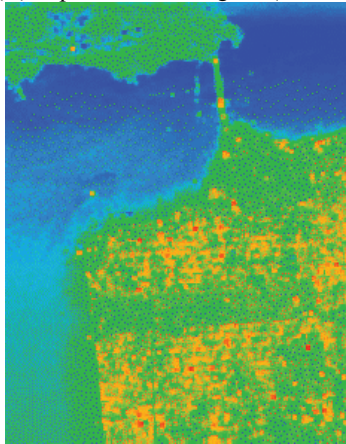
FIGURE 7.21 Speckle filtering effect on the anisotropy (A) values. (A) anisotropy from the original (4-looks); (B) anisotropy from the 5x5 boxcar; (C) anisotropy from the 9x9 boxcar; (D) anisotropy from the refined Lee PolSAR filter.



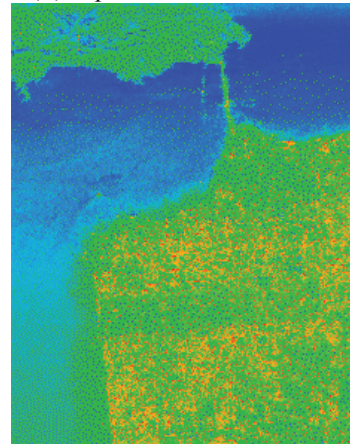
(A) Alpha from the original (4-looks)



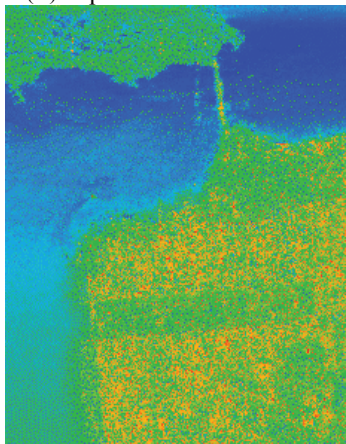
(B) Alpha from the 5×5 boxcar



(C) Alpha from the 9×9 boxcar



(D) Alpha from the refined Lee PolSAR filter



(E) Alpha from the scattering model based filter



(F) Average alpha scale

FIGURE 7.22 Speckle filtering effect on the alpha angle values. (A) Alpha from the original (4-looks); (B) alpha from the 5×5 boxcar; (C) Alpha from the 9×9 box; (D) alpha from the refined Lee PolSAR filter; (E) alpha from the scattering model based filter; and (F) average alpha scale.

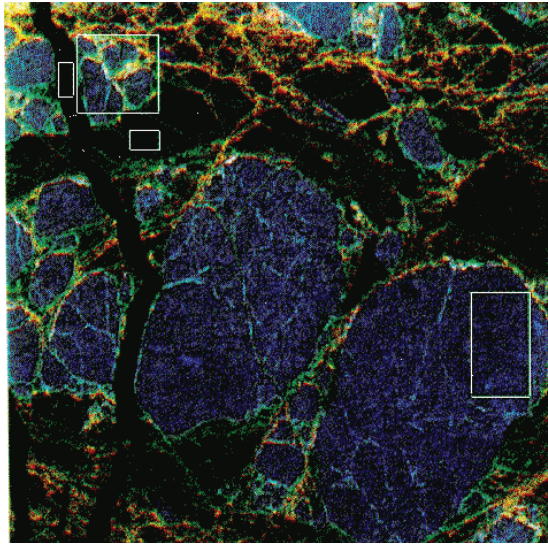


FIGURE 8.1 Original sea ice images in total power with color red=P-band, green=L-band, blue=C-band. Training areas are defined by boxes.

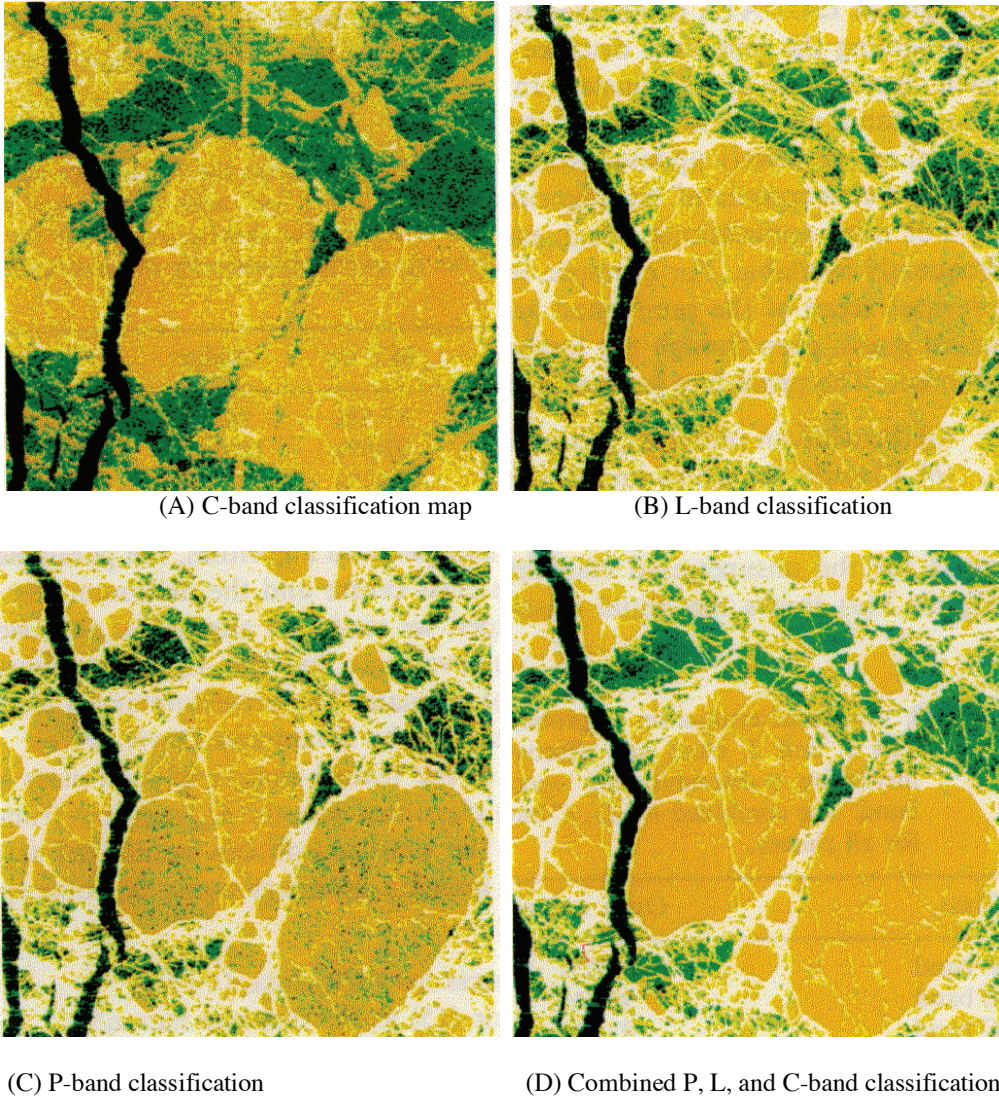
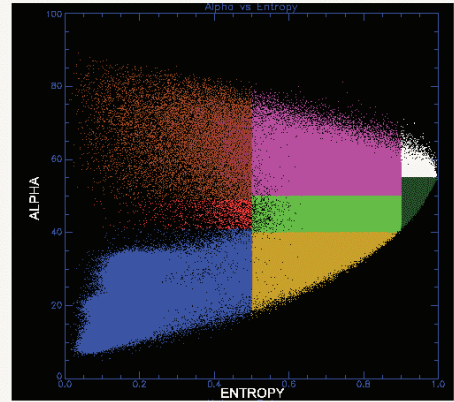


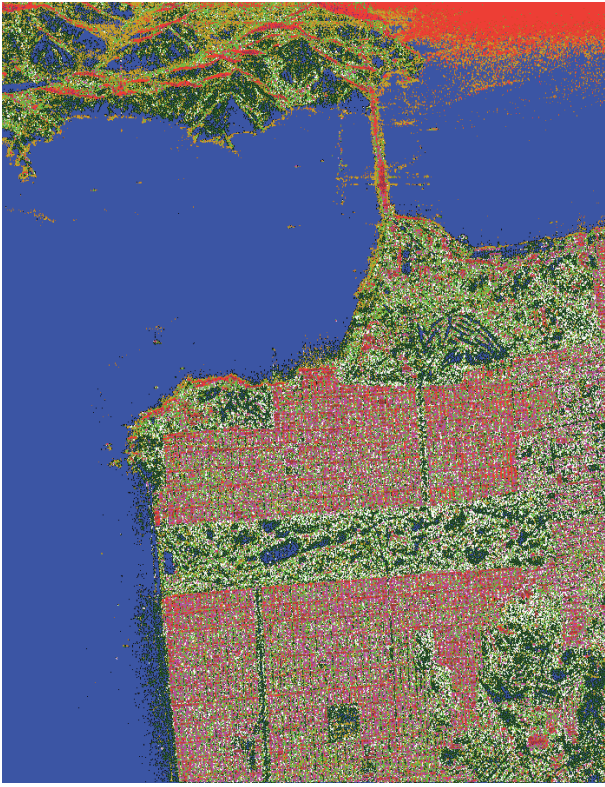
FIGURE 8.2 Results of supervised classification of sea ice polarimetric SAR images. Color assignment is as follows: black = open water, green = FY ice, orange = MY ice, and white = ice ridges.



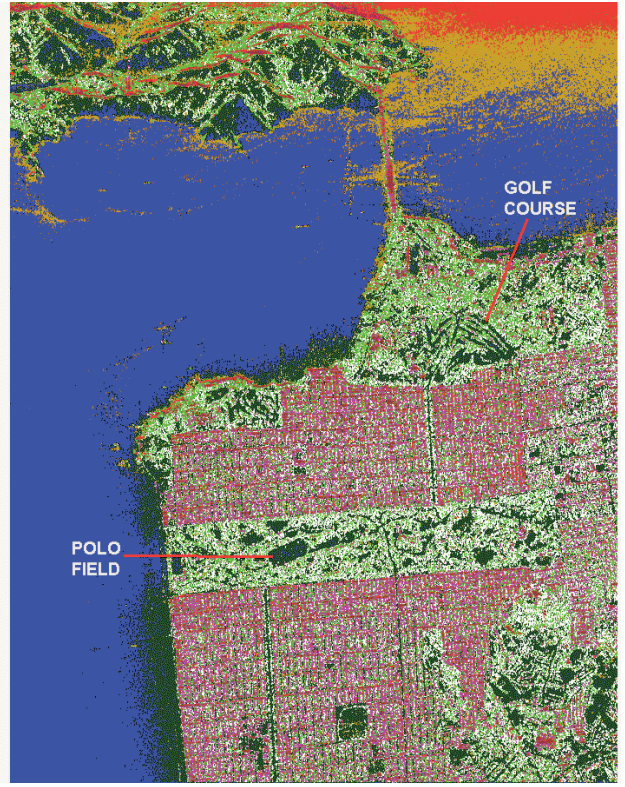
(A) Classification Map of the San Francisco scene based on alpha and entropy

(B) Color code for each zone

FIGURE 8.3 Classification based on target decomposition in alpha and entropy plane.



(A) After two iterations



(B) After four iterations

FIGURE 8.4 Classification by the new unsupervised method after two and four iterations.

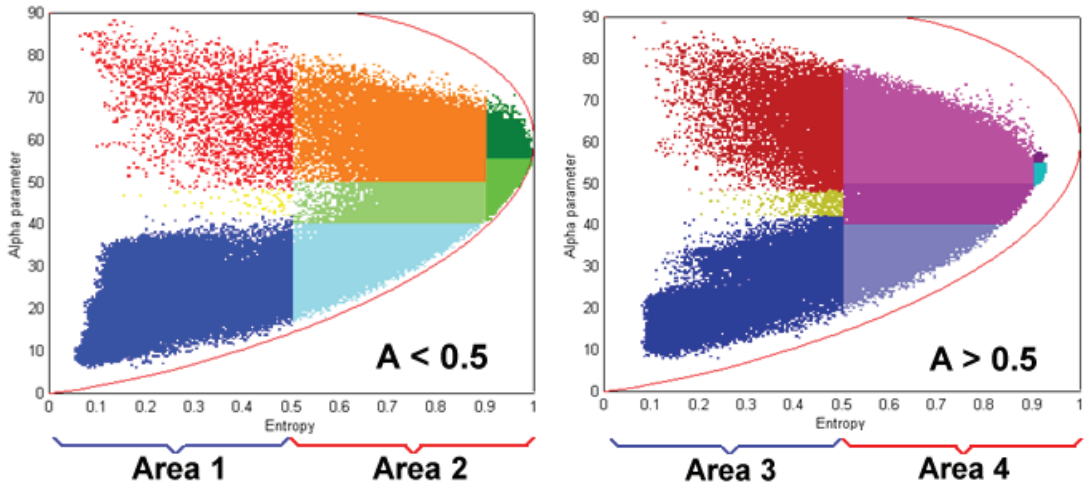


FIGURE 8.6 Distribution of the San Francisco bay PolSAR data in $H/\bar{\alpha}$ plane corresponding to anisotropy $A < 0.5$ and $A > 0.5$. The $H/\bar{\alpha}$ planes are further divided into four areas.



FIGURE 8.7 Classification results after applying anisotropy and the Wishart classifier applied for four iteration.

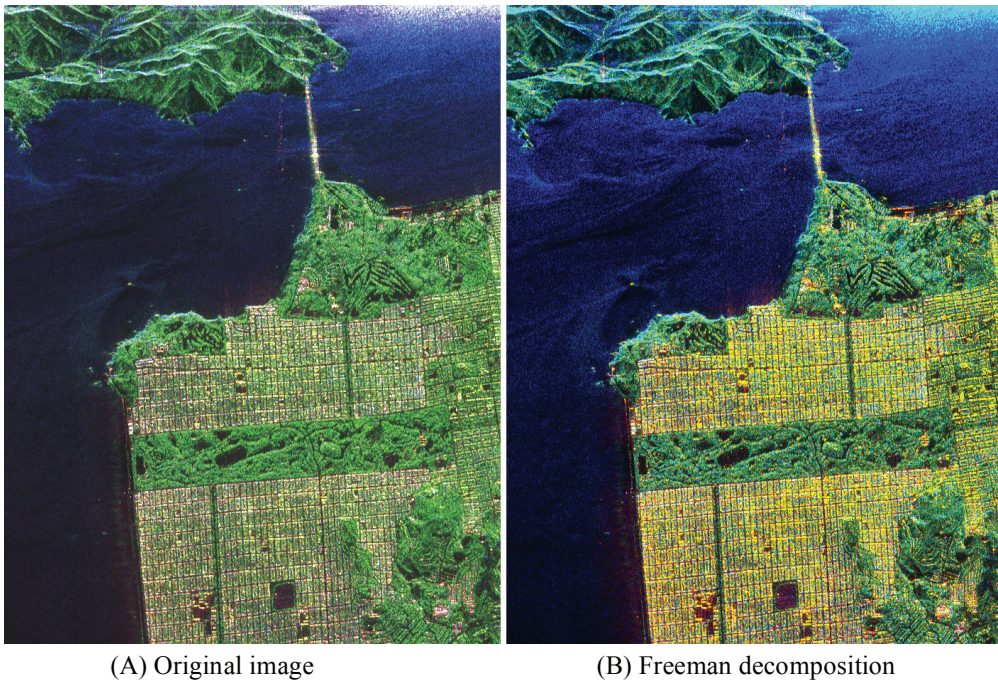


FIGURE 8.9 The characteristics of Freeman and Durden decomposition. (A) NASA JPL POLSAR image of San Francisco displayed with Pauli matrix components: $|HH\ VV|$, $|HV|$, and $|HH + VV|$, for red, green, and blue, respectively. (B) The Freeman and Durden decomposition using $|P_{DB}|$, $|P_V|$, and $|P_S|$ for red, green, and blue. The Freeman and Durden decomposition possesses similar characteristics to the Pauli-based decomposition, but provides a more realistic representation, because it uses scattering models with dielectric surfaces. In addition, details are sharper.

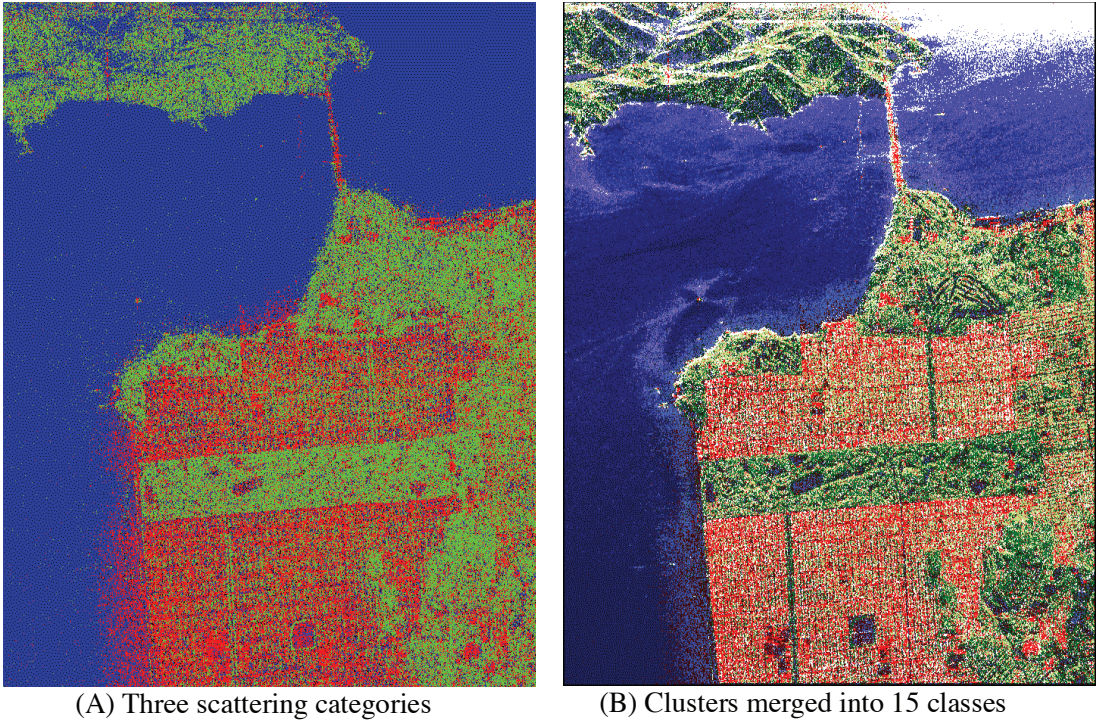


FIGURE 8.10 Scattering categories and the initial clustering result. (A) The scattering category map shows double bounce scattering in red, volume scattering in green, and surface scattering in blue. (B) The initial cluster result merged into 15 classes with each class coded according to the color map of Figure 8.11B.

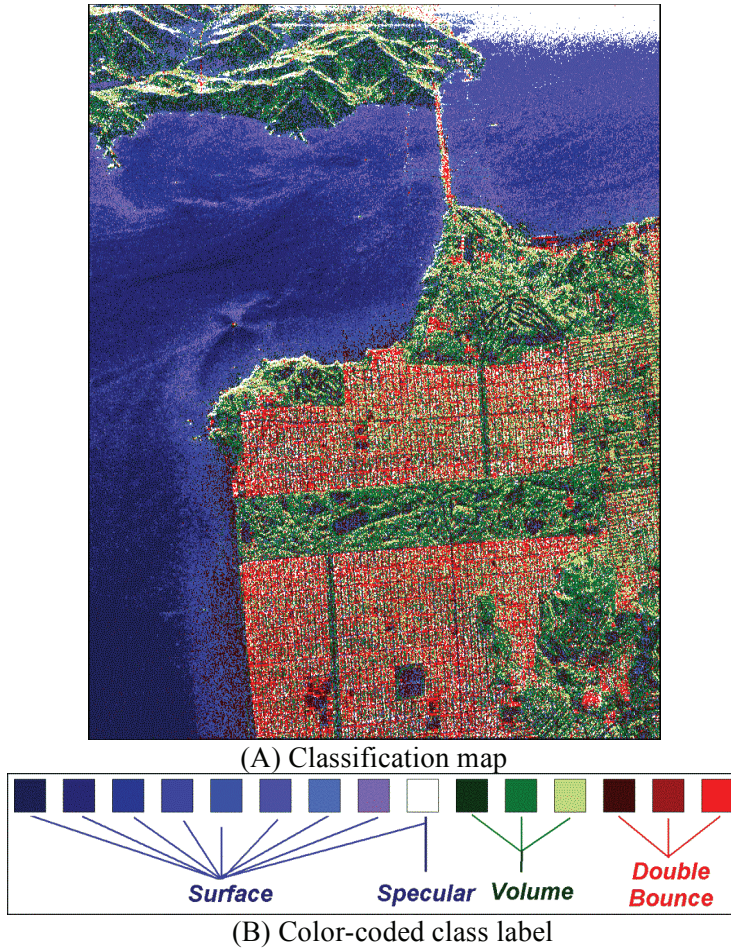
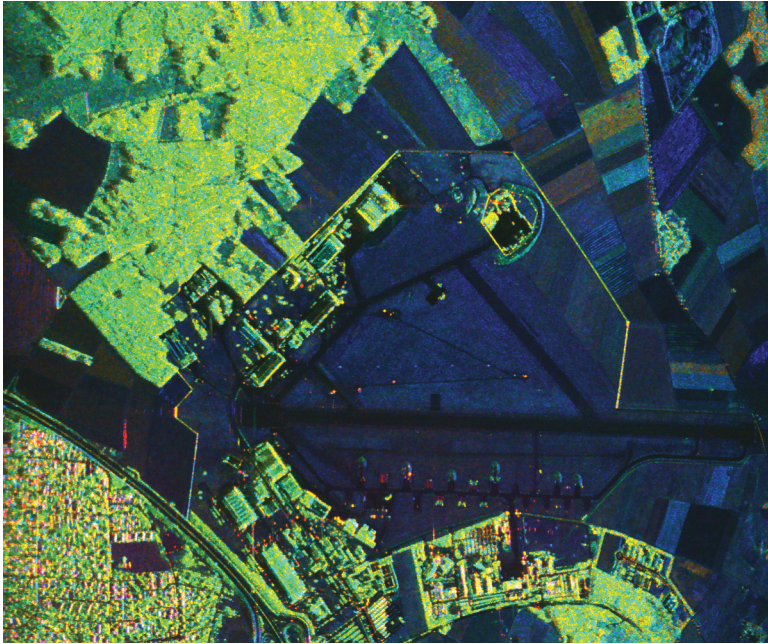
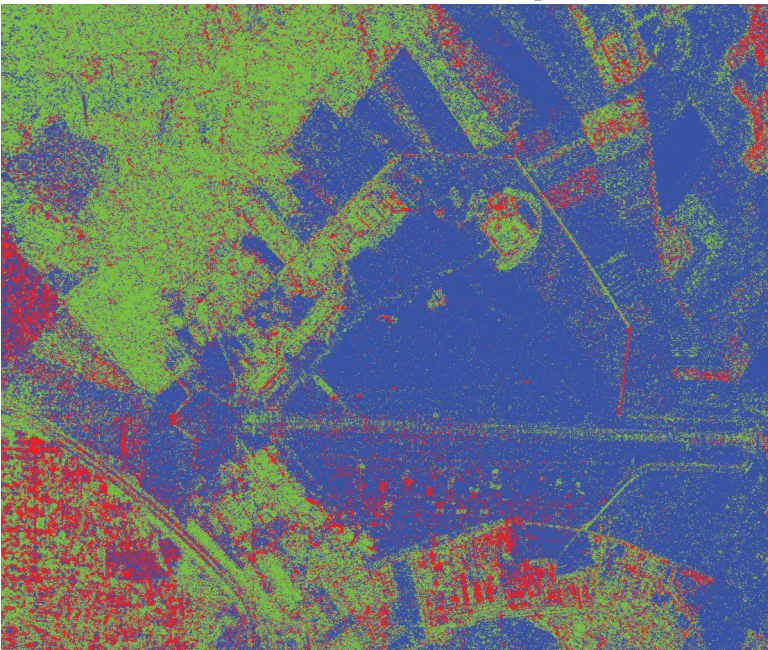


FIGURE 8.11 Classification map and automated color rendering for classes. (A) The final classification map of the San Francisco image into 15 classes after the fourth iteration. (B) The color-coded class map. We have 9 classes with surface scattering because of the large ocean area in the image. The specular class includes the ocean surface at the top right area because of small incidence angles, and there are many specular returns in city blocks. Three volume classes detail volume scattering from trees and vegetation. The double bounce classes clearly show street patterns associated with the city blocks, and double bounce classes are also scattered through the park areas.

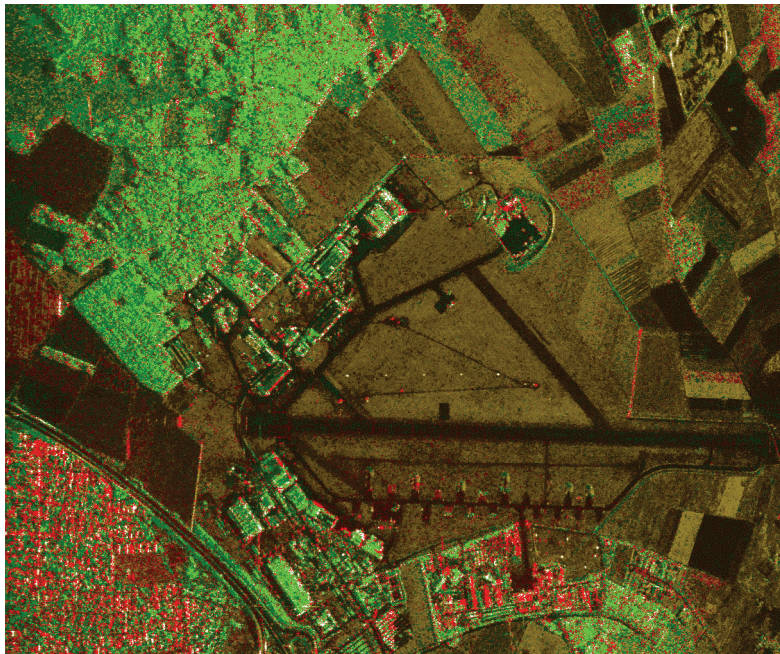


(A) Freeman and Durden Decomposition

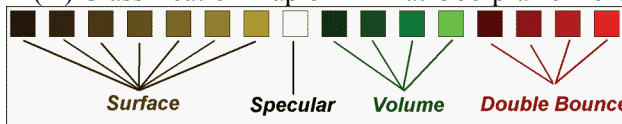


(B) Three scattering categories

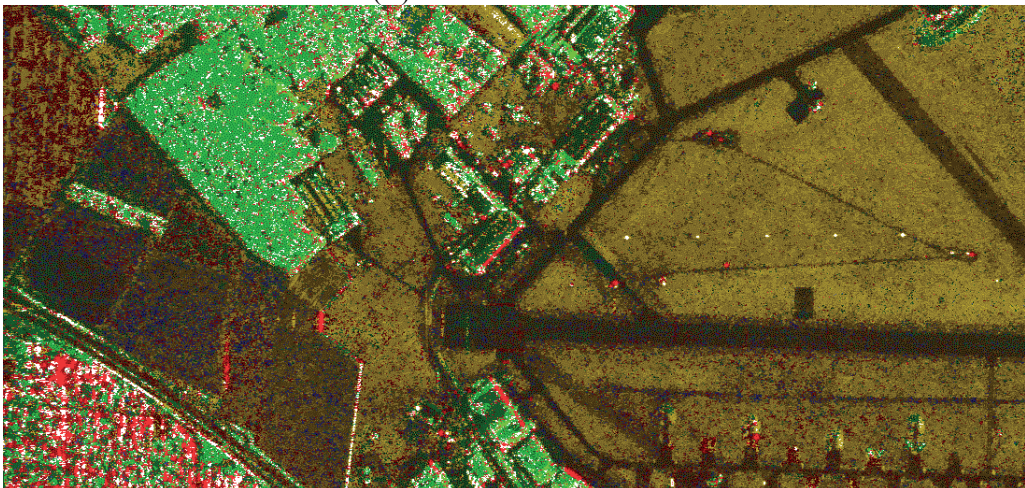
FIGURE 8.12 Freeman decomposition applied to the DLR E-SAR image of Oberpfaffenhofen. (A) The Freeman and Durden decomposition result with double bounce, volume, and surface amplitudes displayed as red, green and blue composite colors. (B) The scattering category map with double bounce scattering in red, volume scattering in green, and surface scattering in blue.



(A) Classification map of DLR at Oberpfaffenhofen



(B) Color-coded class label



(C) Zoomed up area to show details

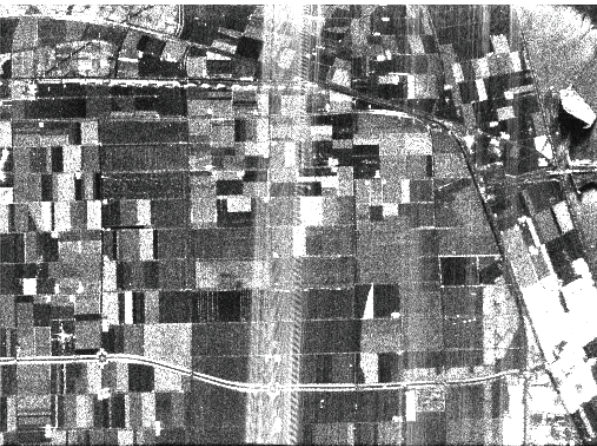
FIGURE 8.13 The DLR=E-SAR data classification result. (A) The classification map of 16 classes. (B) The color-coded class label. Here, we applied a different color-coding for classes in the surface scattering category. We use brown surface colors to better represent the nature of this image because of the absence of any large body of water. The vegetation and forest are well classified. We observe in the zoomed up area (C) that five trihedrals in the triangle inside the runway are clearly classified in the specular scattering class shown in white. Also, dihedrals with double bounce are shown in red.



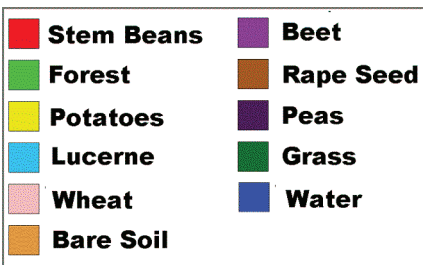
(A) Original L-Band image



(B) Original ground truth map

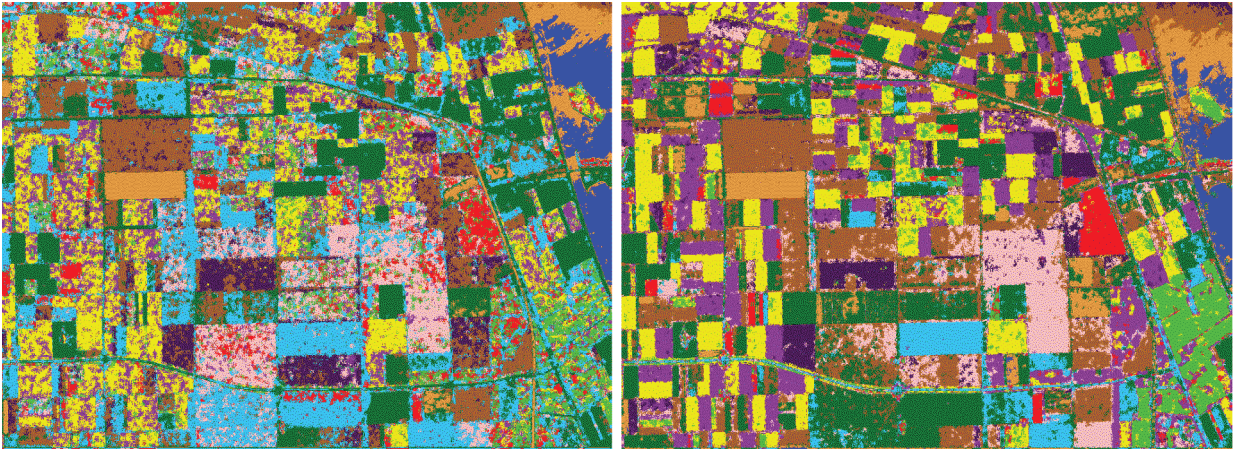
(C) P-Band $|VV|$ image

(D) Training sets and reference map



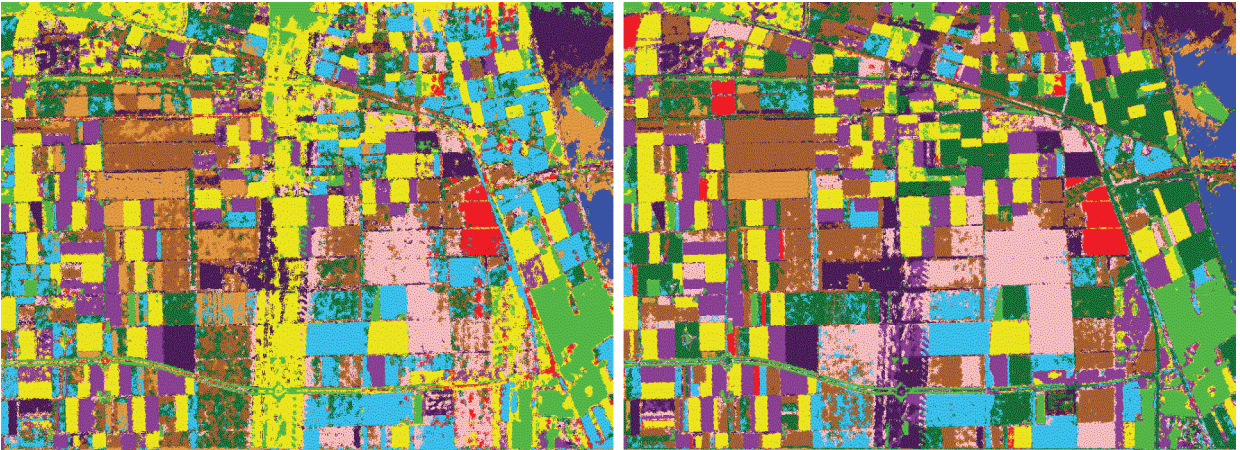
(E) Class Label

FIGURE 8.14 L-band polarimetric SAR image of Flevoland, Netherlands, and its ground truth map for crop classification. (A) original L-band image with color composition by Pauli matrix representation: Red for $|HH - VV|$, green for $|HV| + |VH|$, and blue for $|HH + VV|$. (B) Original ground truth map. A total of 11 classes are identified. (C) P-band $|VV|$ image. Bright noisy strips are probably due to radio frequency interference. (D) The modified training set. (E) Color-coded class label.



(A) C-Band fully polarimetric classification classification

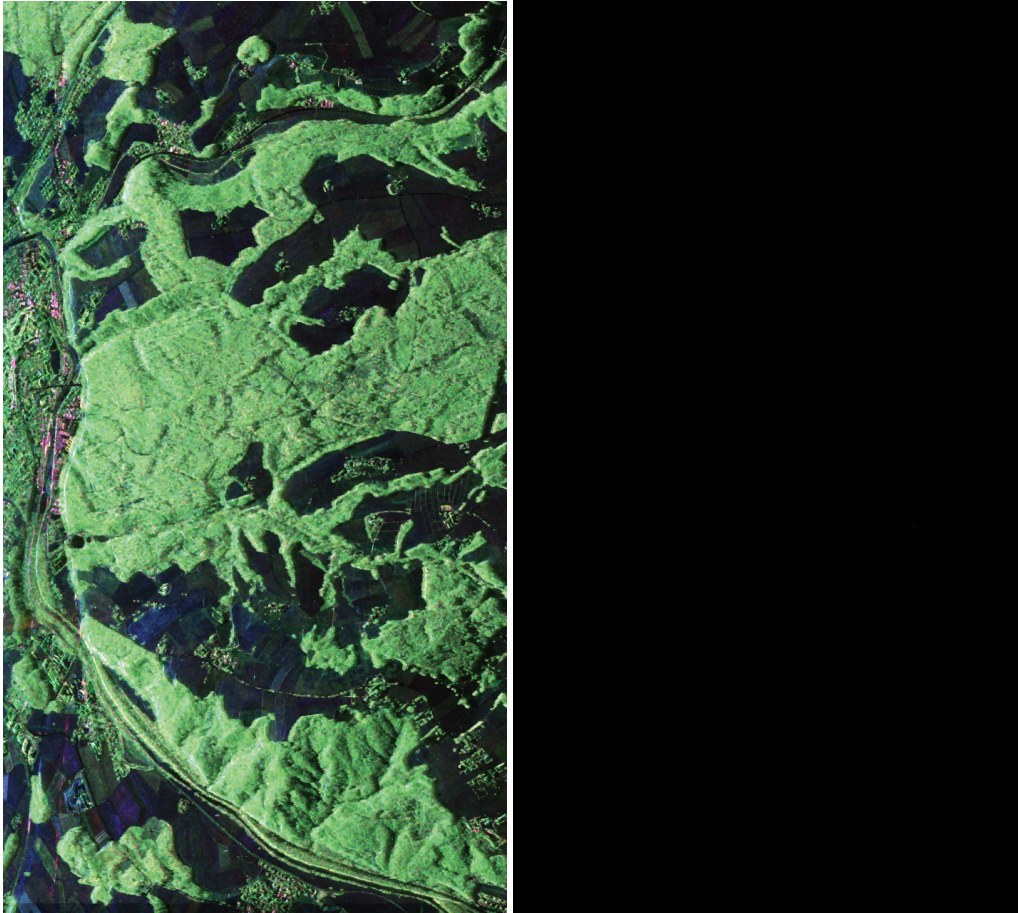
(B) L-Band fully polarimetric



(C) P-Band fully polarimetric classification result

(D) Combined P-,L-,C-Band fully polarimetric

FIGURE 8.15 Comparisons of fully polarimetric SAR crop classification results. (A) C-band fully polarimetric classification result. The overall correct classification rate is 66.53%. (B) L-band fully polarimetric classification result with overall rate of 81.63%. (C) P-band fully polarimetric classification result with overall rate of 71.37%. (D) Combined P-, L-, C-band classification with overall rate at 91.21%.



(A) Pauli vector color coded image

(B) Unsupervised PolSAR classification



(C) Class label for classification based on scattering mechanisms

FIGURE 9.1 L-band E-SAR data of Traunstein test site. The Pauli vector, $|HH - VV|$, $|HV|$, and $|HH + VV|$ is displayed as RGB in (A). Unsupervised scattering model-based classification result based on PolSAR data alone depicts the segmentation of volume scattering classes of forested areas in (B). The class label is shown in (C).

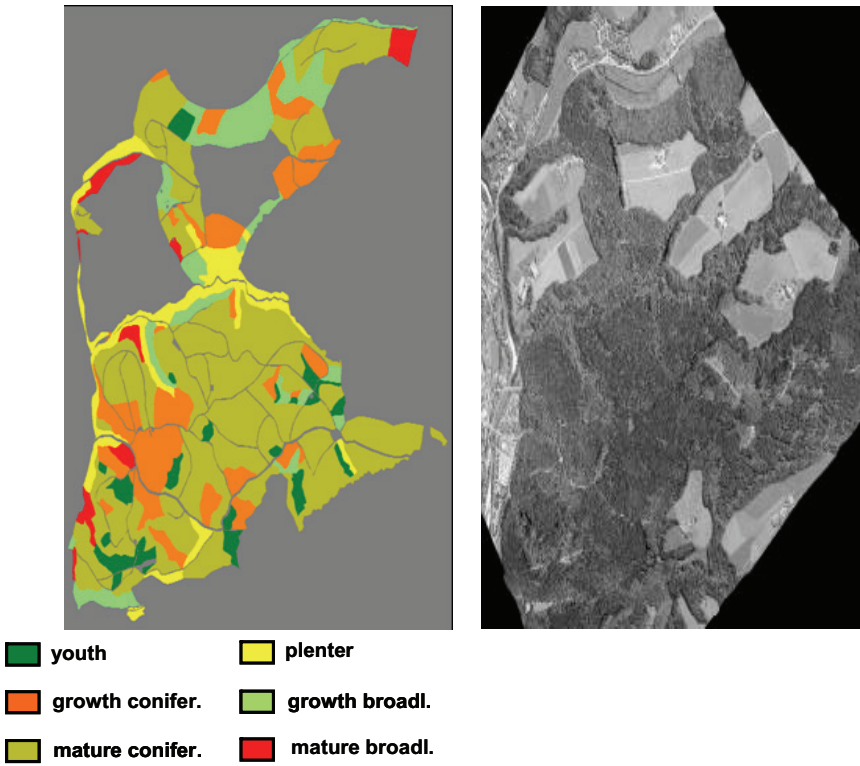


FIGURE 9.2 Ground measurements and ortho-rectified photo of the Traunstein experiment area. (Courtesy of Dr. K. Papathanassiou—DLR-HF.)

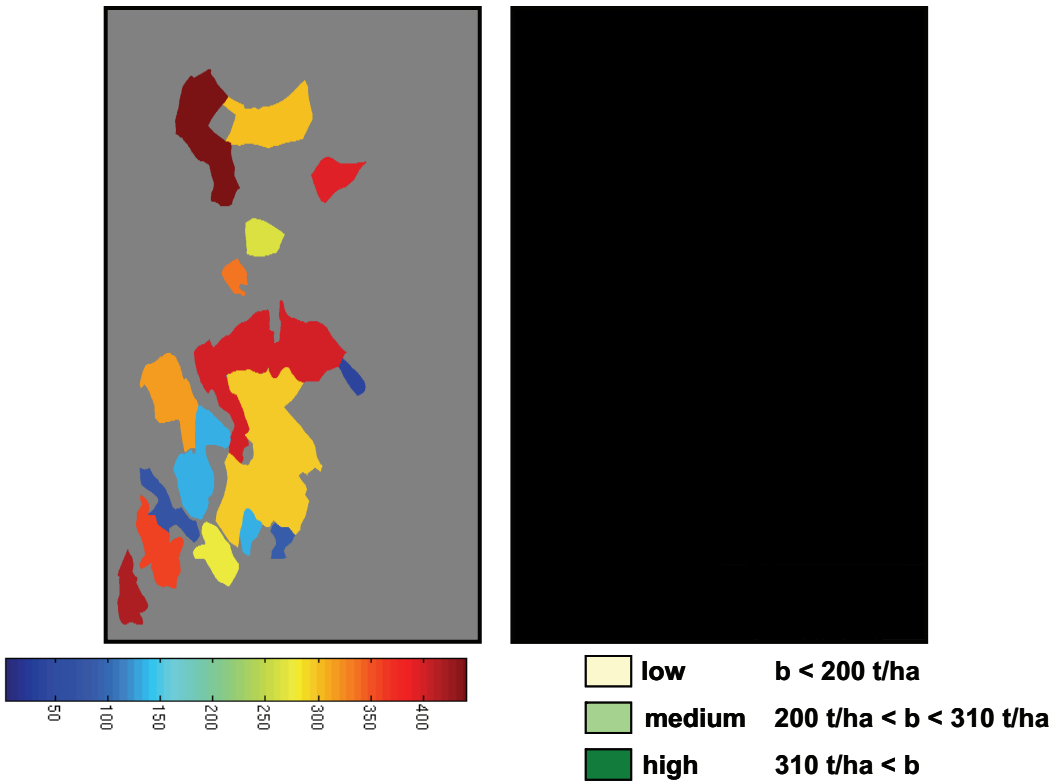


FIGURE 9.3 Simplified biomass ground truth of the Traunstein experiment area. (Courtesy of Dr. K. Papathanassiou—DLR-HF.)

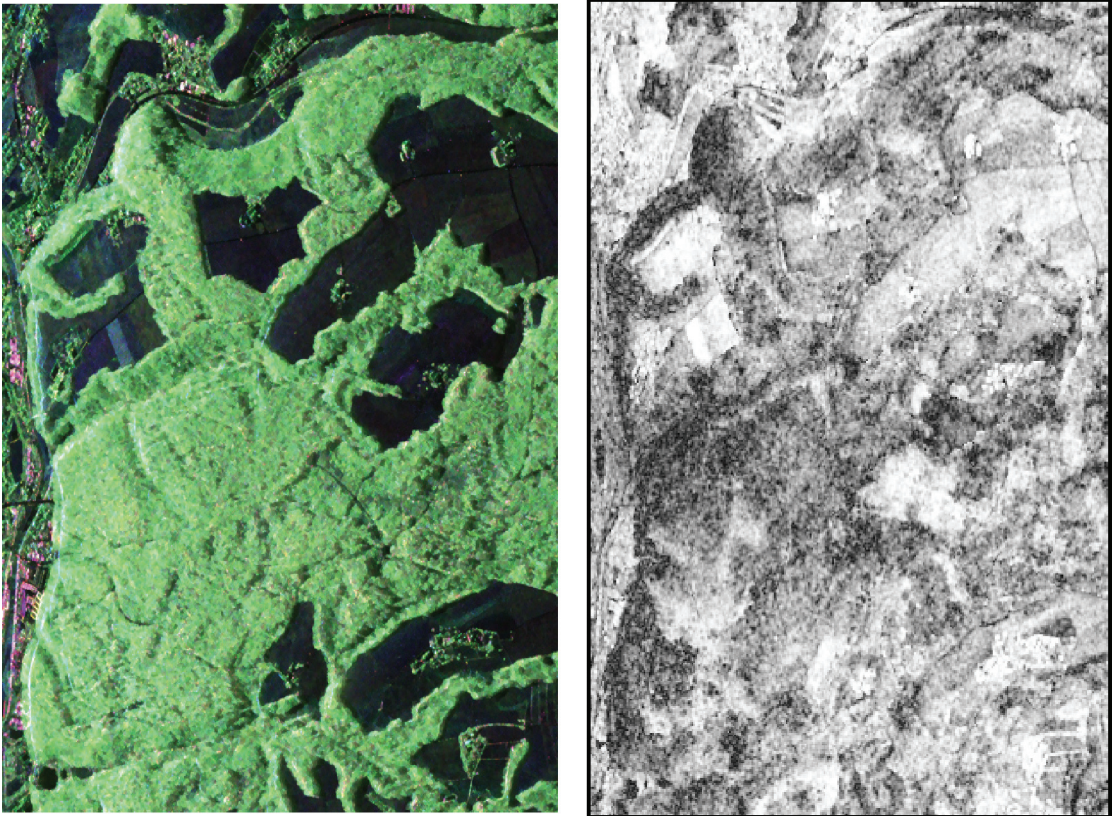


FIGURE 9.4 Polarimetric Pauli color-coded and interferometric coherence images over the Traunstein experiment area.

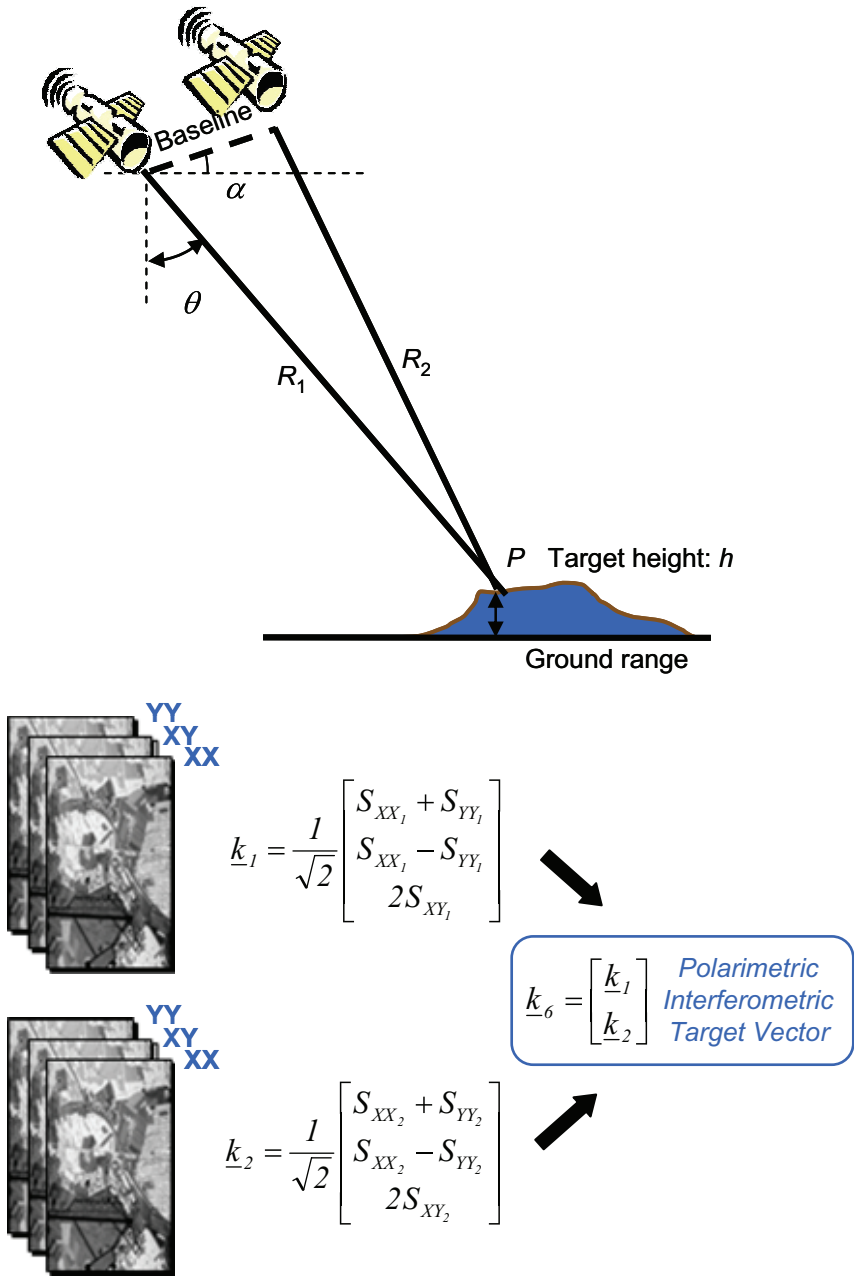


FIGURE 9.5 Polarimetric interferometric acquisition geometry.

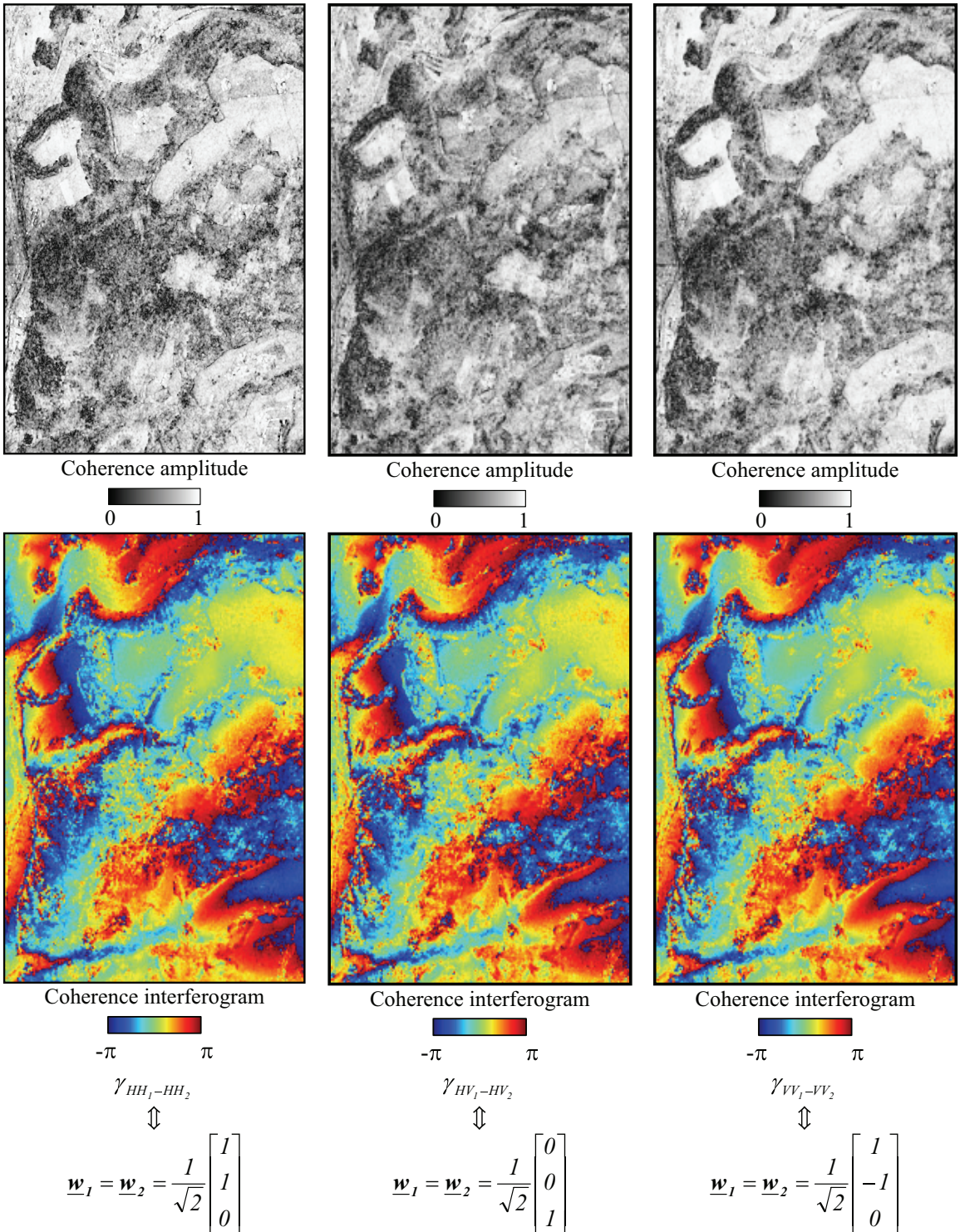


FIGURE 9.6 Complex coherences for linear polarization channels.

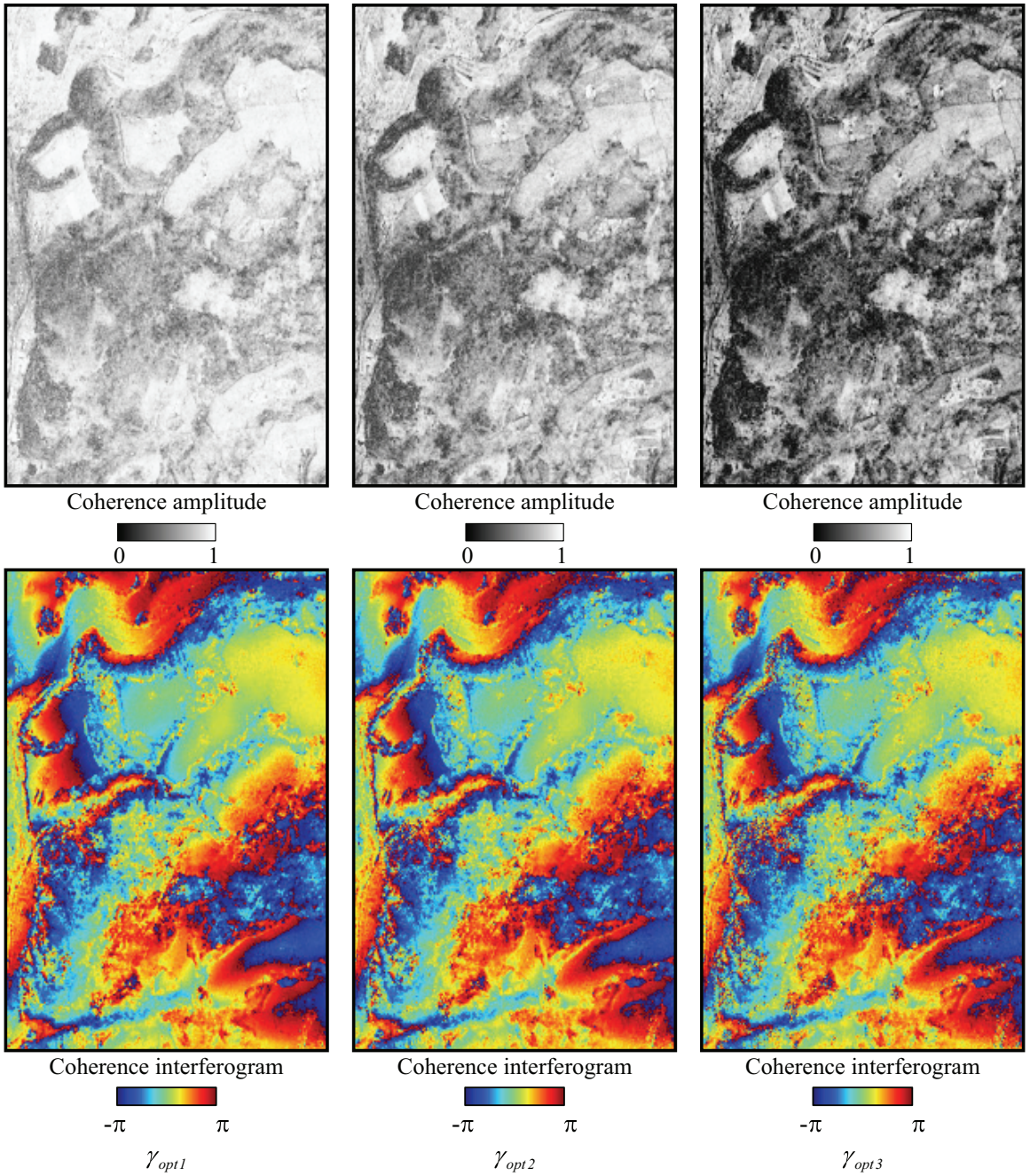


FIGURE 9.7 Optimal complex coherences are shown. The magnitudes of coherences are in the first row and interferometric phases are in the second row.

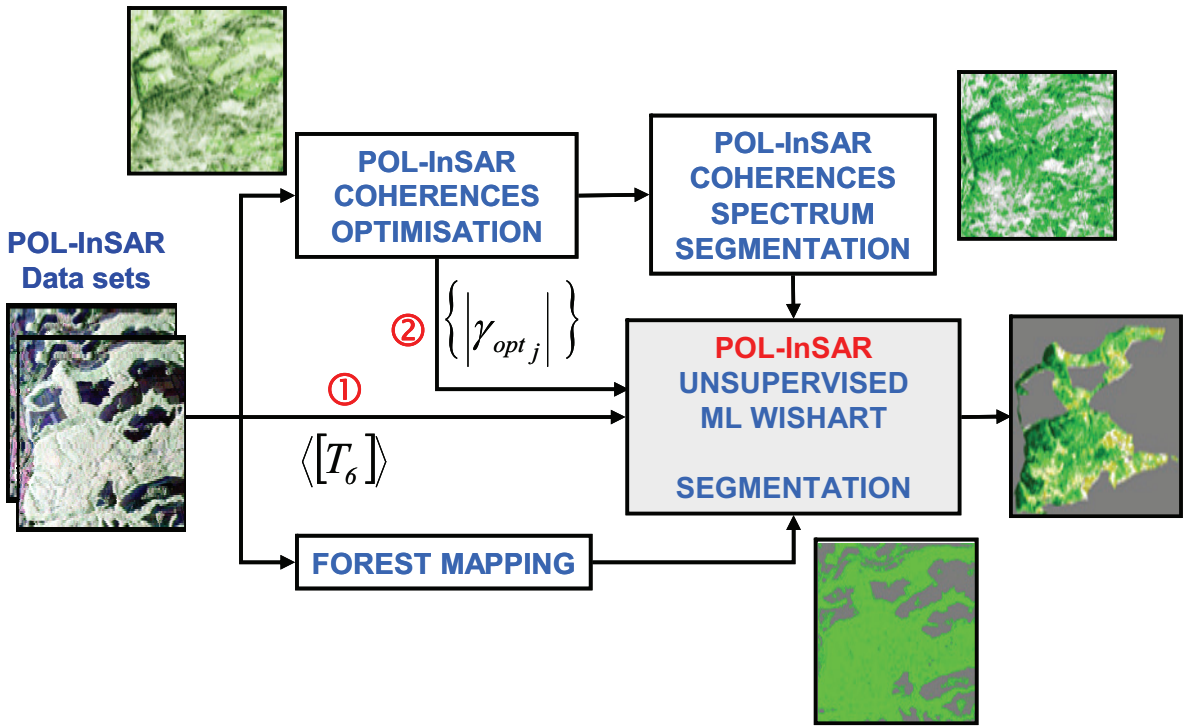


FIGURE 9.8 Unsupervised Pol-InSAR segmentation procedures: (1) based on the complex 6×6 coherency T_6 matrix and (2) based on the optimal coherence set $\{|\gamma_{opt-j}|\}$.

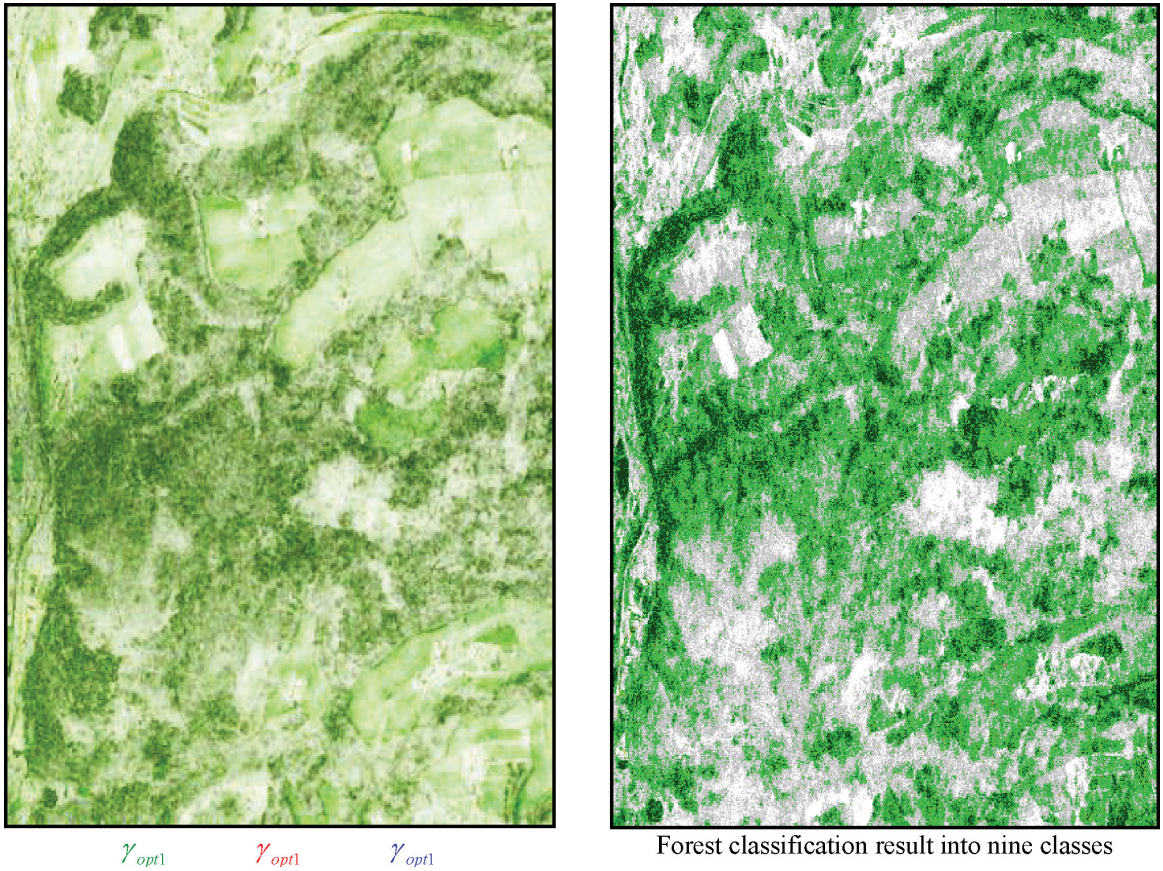


FIGURE 9.9 (A) Optimal coherence set color-coded image and (B) the classification results based on normalized optimal coherence into nine classes by the zones in the A_1 - A_2 plane of Figure 9.10. The nine classes are coded by the color associated with each zone in the A_1 - A_2 plot.

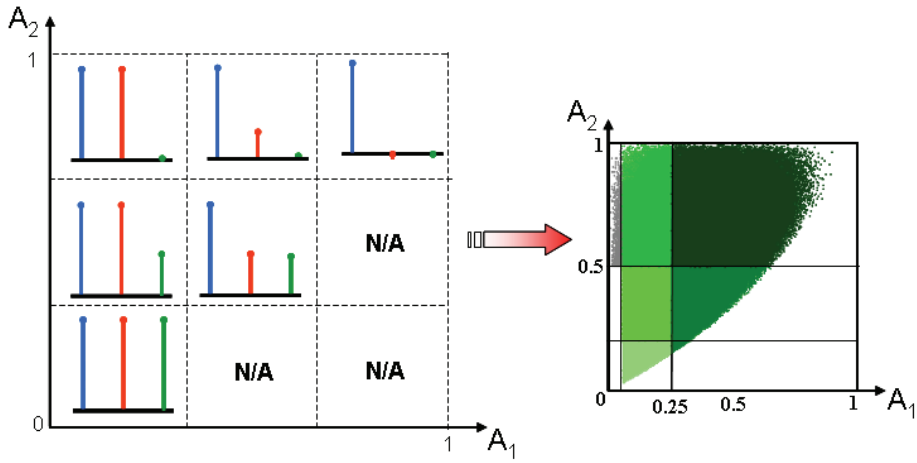


FIGURE 9.10 Discrimination of different optimal coherence set using A_1 and A_2 (left). Selection in the A_1 - A_2 plane (right).

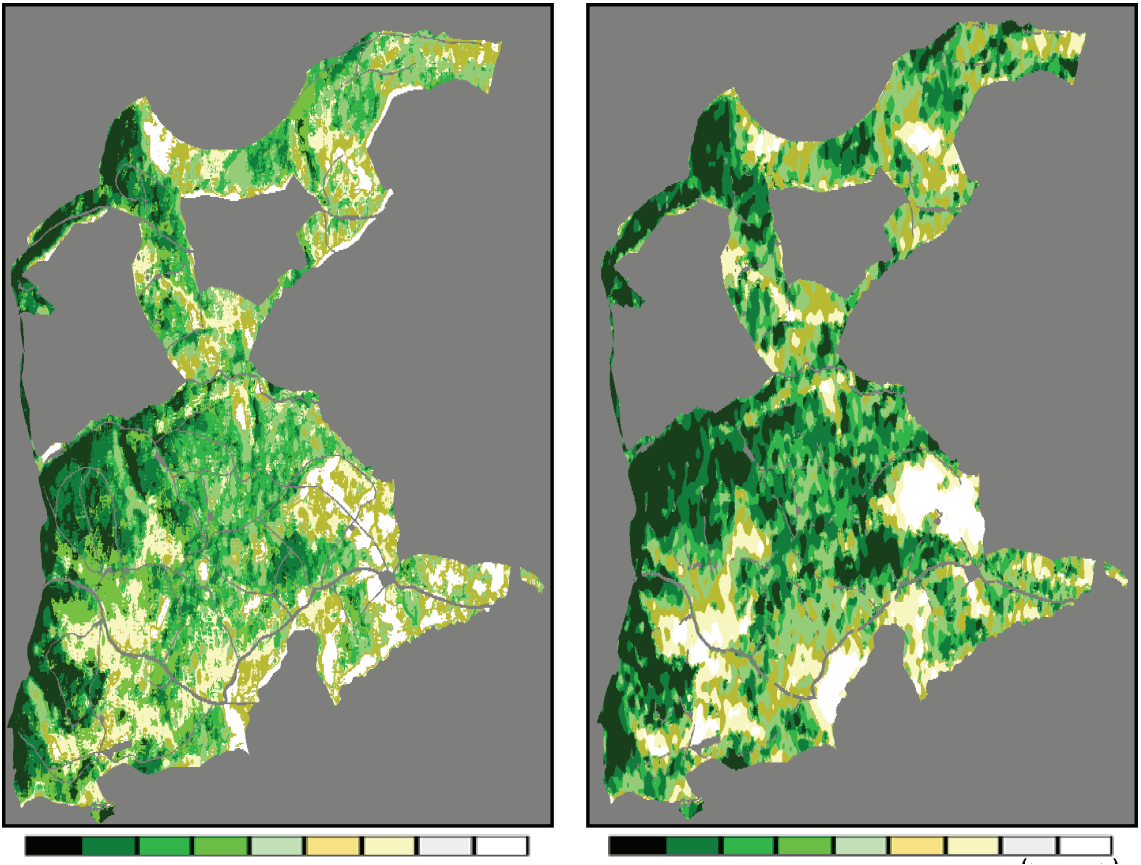


FIGURE 9.11 Unsupervised Pol-InSAR segmentation based on the T_6 statistics (left) and the $\{|\gamma_{opt-j}|\}$ statistics (right). (Spatial baseline = 5 m, temporal baseline = 10 min.)

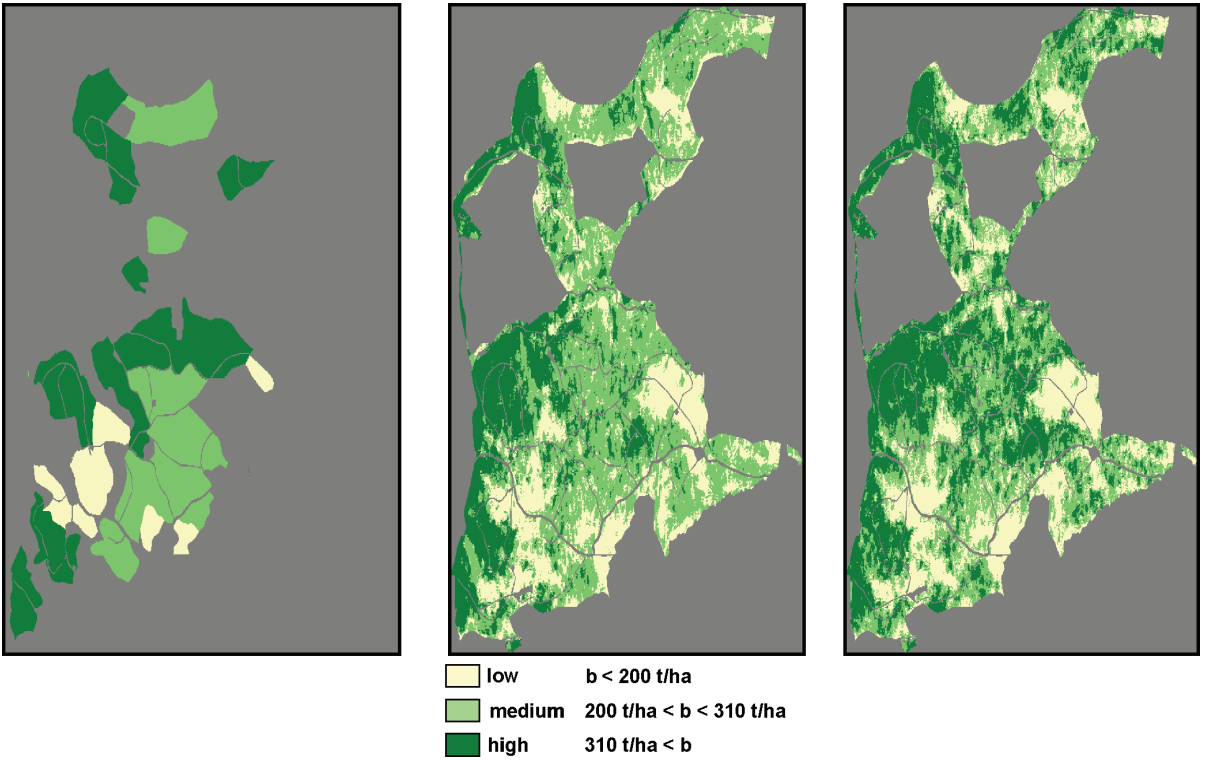


FIGURE 9.12 The biomass ground truth map is shown on the right. Supervised Pol-InSAR biomass classification based on the T_6 statistics (middle) and the $\{ly_{opt-j}\}$ statistics (right). (Spatial baseline = 5 m, temporal baseline = 10 min.)



FIGURE 10.1 EMISAR image of Great Belt Bridge, Denmark during construction. PolSAR signature is displayed with Pauli vector color code.

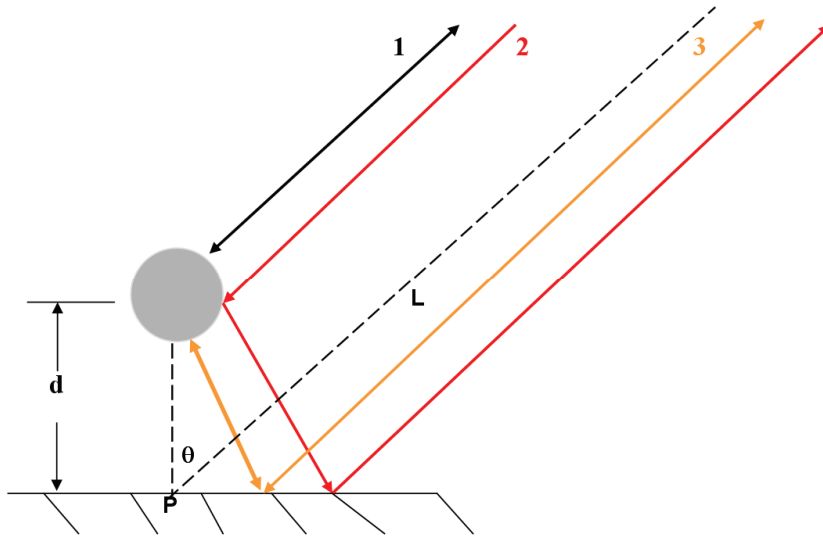
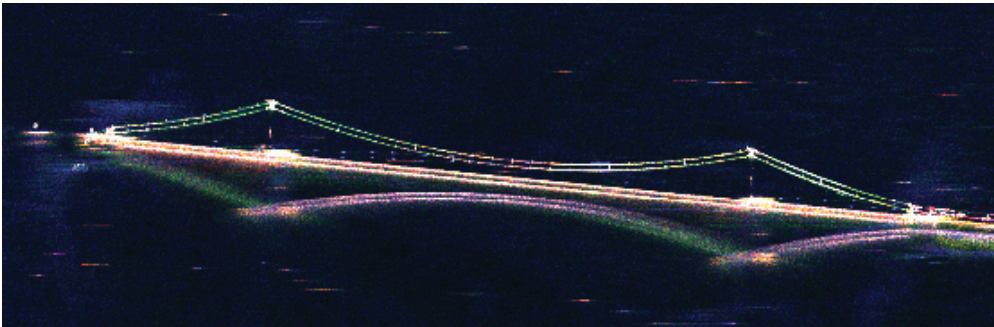


FIGURE 10.2 The path denoted by “3” is a case of the triple bounce scattering, and path “1” and path “2” are single bounce and double bounce, respectively. It can be easily proved that the roundtrip distance of the single bounce return is $2(L - d \cos \theta)$, the roundtrip distance of the double bounce return is $2L$, and the roundtrip distance of the triple bounce return is $2(L + d \cos \theta)$. The parameter θ is the local incidence angle.

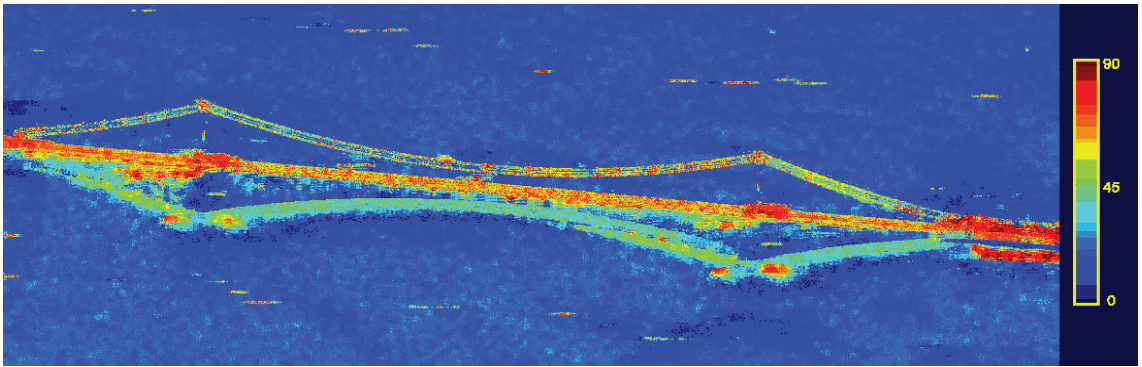


(A) Aerial photo



(B) Pauli decomposition

FIGURE 10.4 During construction, the deck was not installed as shown in an aerial photo (A). The Pauli vector display (B) of the POLSAR data, using $|HH - VV|$, $|HV|$, and $|HH + VV|$ as red, green, and blue, respectively, separates the dihedral, cross-pol, and surface scattering.

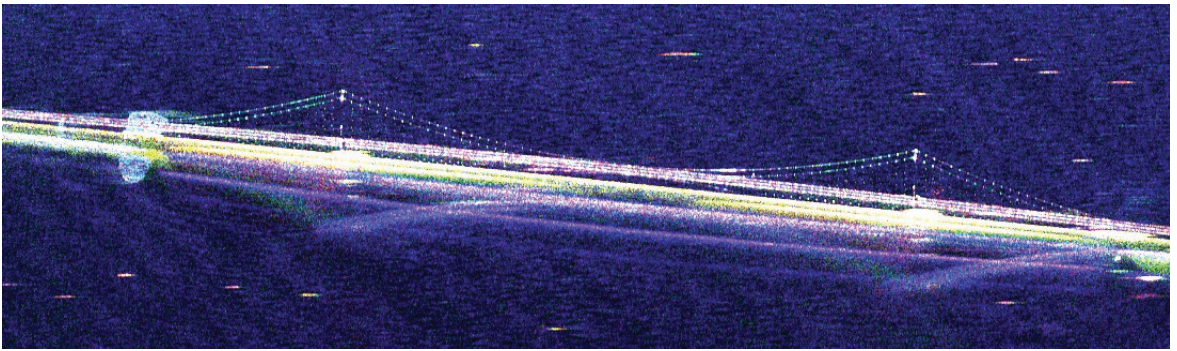


Averaged alpha angle

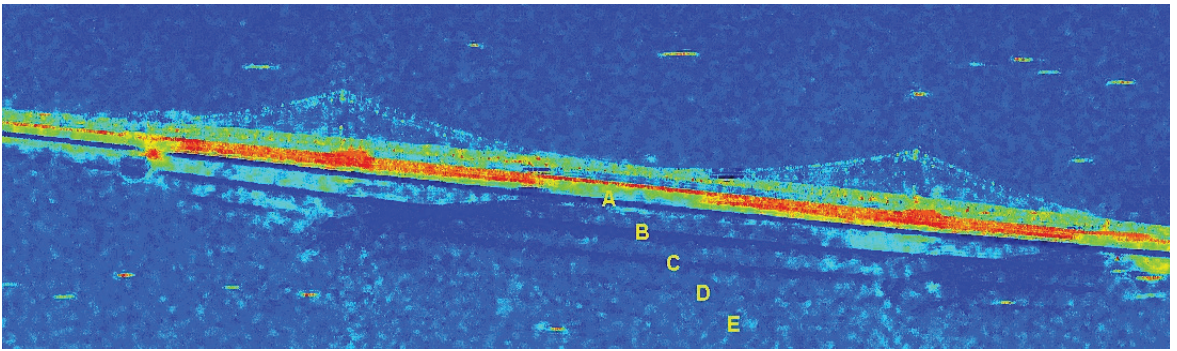
FIGURE 10.5 The averaged alpha angle of the Cloude and Pottier decomposition with a color scale between $[0^\circ, 90^\circ]$ is shown on the right.



(A) An aerial photo of the bridge after completion



(B) Pauli decomposition



(C) Average alpha angle

FIGURE 10.7 Images after the completion of bridge construction. An aerial photo is shown in (A). The Pauli decomposed image (B) shows the bridge signatures very different from those during construction. The average alpha angle image obtained by the Cloude–Pottier decomposition is shown in (C). The triple bounce from the deck is denoted as “A” in figure (C). The other parallel signatures denoted by “B”, “C”, “D”, and “E” are induced by higher order of multiple odd bounces from the deck and the ocean surface.



FIGURE 10.10 This photo shows the topography and vegetation in Camp Roberts, California.

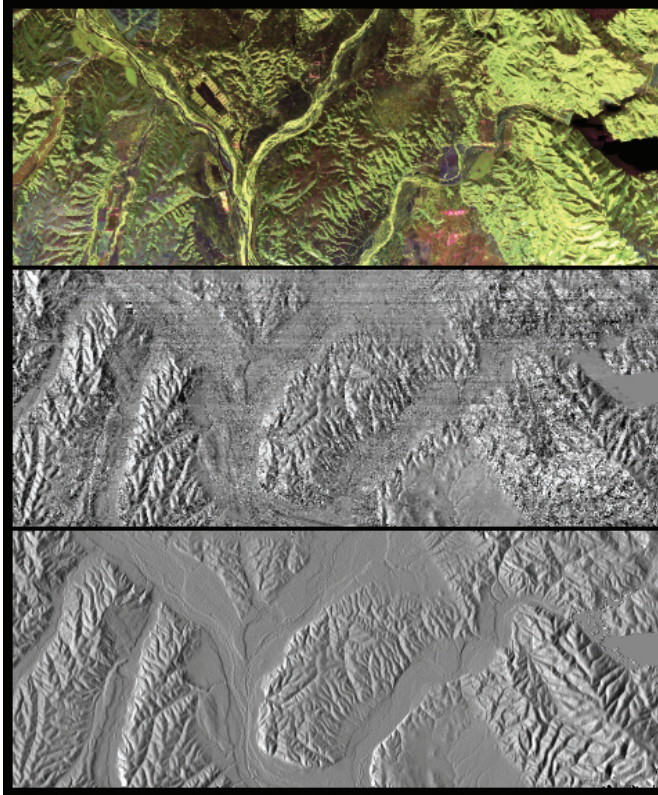


FIGURE 10.11 The top image shows the PolSAR data of Camp Roberts. The middle image shows polarization orientation angles derived by the circular polarization method. For comparison, the lower image shows orientation angles derived from a DEM, generated by C-band interferometric SAR. These two images are strikingly similar, except for the streaking in the middle image due to instrument noise.

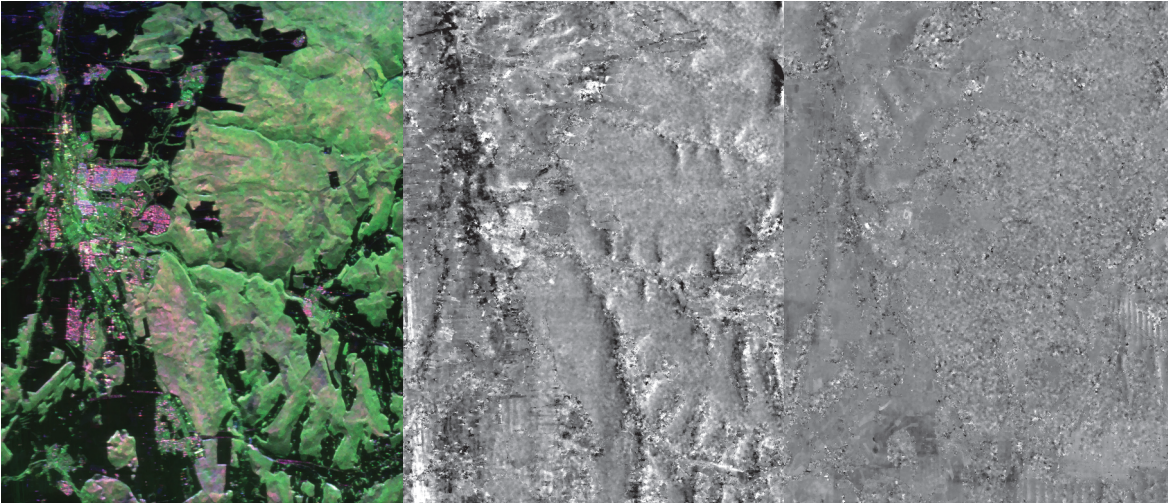
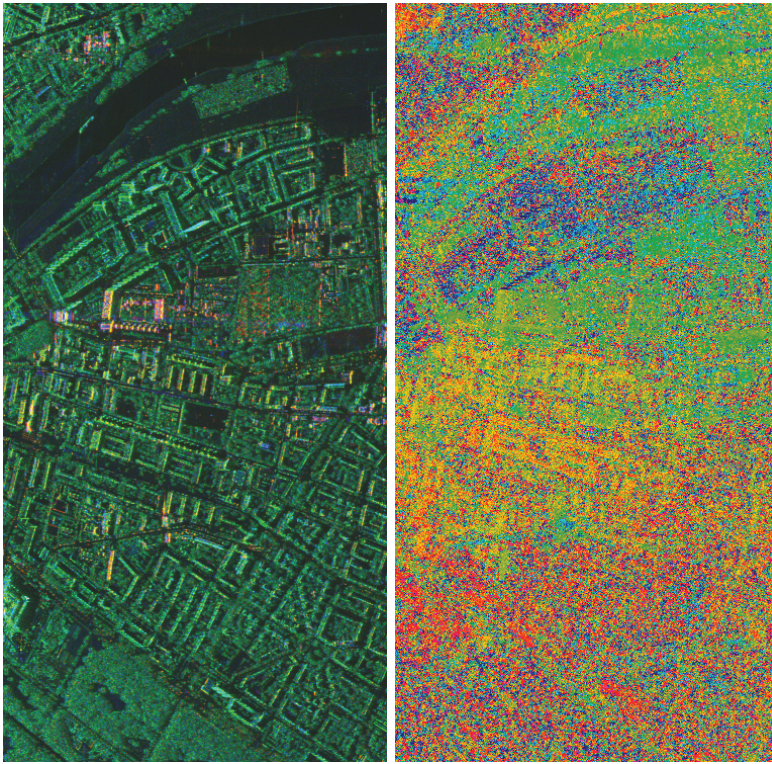
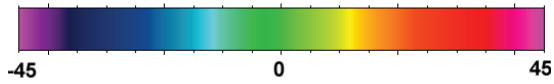


FIGURE 10.13 In heavily forested areas, orientation angles can be extracted from P-band data, but not from L-band or higher frequency data. JPL AIRSAR P-band and L-band data of forests near Freiburg, Germany, is applied to extract orientation angles. (A) $|HH - VV|$, $|HV|$, and $|HH + VV|$ color-coded P-Band SAR image, (B) Orientation angle image derived from the P-band data, (C) Orientation angle image derived from the L-band data.



(A) Pauli vector color coding (B) Orientation angle



(C) Color label for orientation angle

FIGURE 10.16 Building orientation angle estimation.

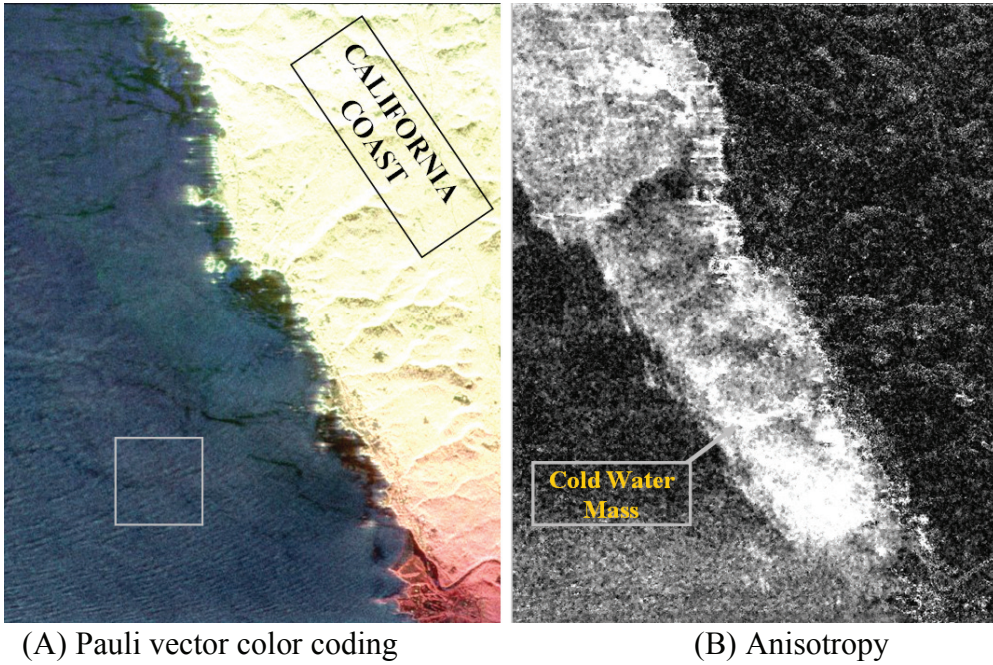
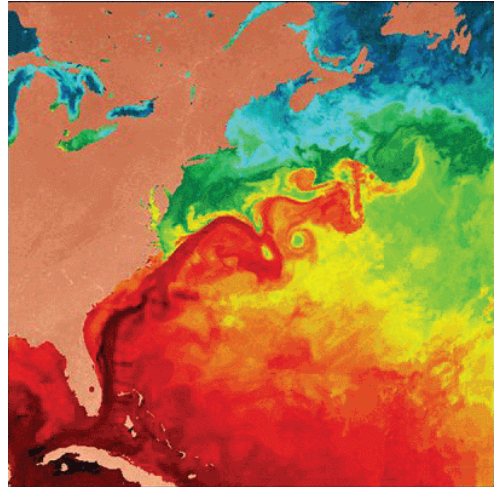


FIGURE 10.17 AIRSAR data (1224×1279 pixels) of Gualala River, California is used for illustration. Sea surface roughness correlates with anisotropy shown in bright water area in (B). The cold water mass has a smoother surface, and is clearly detected by the anisotropy. Anisotropy is a measure of surface small-scale roughness: $k_s = 1 - A$. The highlighted ocean area in (A) will be used to study ocean slope spectra.



(A) AVHRR image of Gulf Stream

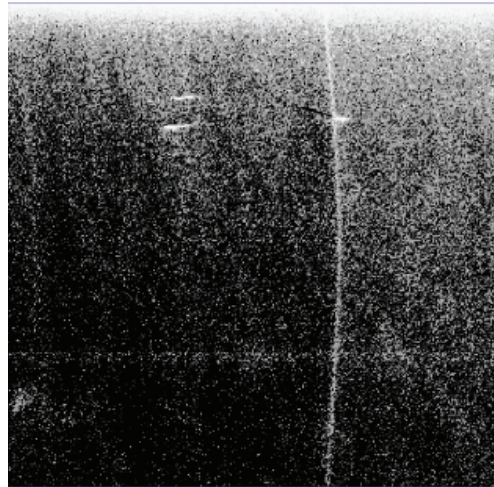
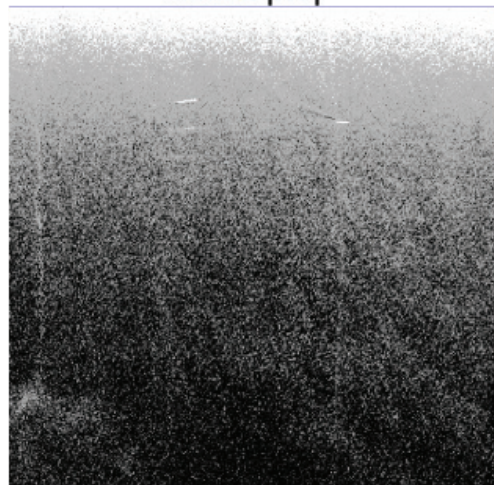
L-Band $|HV|$ L-Band $|VV|$

FIGURE 10.18 A wide area AVHRR image of sea surface temperature (A) shows the warm Gulf Stream (red) along the coast and then gyrating out to sea. The $|HV|$ and $|VV|$ L-band SAR images are shown in figures B and C, respectively.

(B) L-band HH and VV images

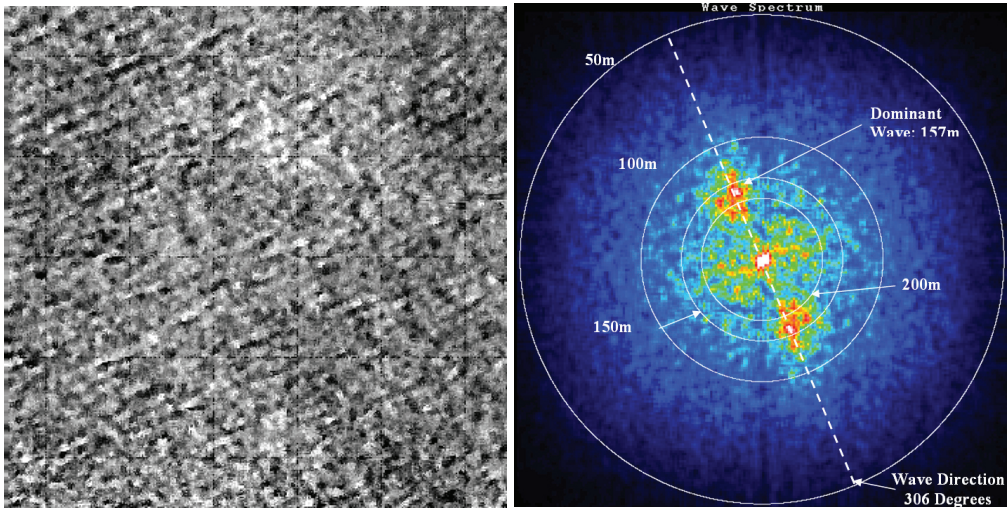


FIGURE 10.20 Orientation angle spectra versus wave number for azimuth direction waves propagating through the study site. The white rings correspond to 50, 100, 150, and 200 m. The dominant wave, of wavelength 157 m, is propagating at a heading of 306° . The study area is highlighted in Figure 10.17A. (A) Polarization angle image, (B) Orientation angle wave spectrum.

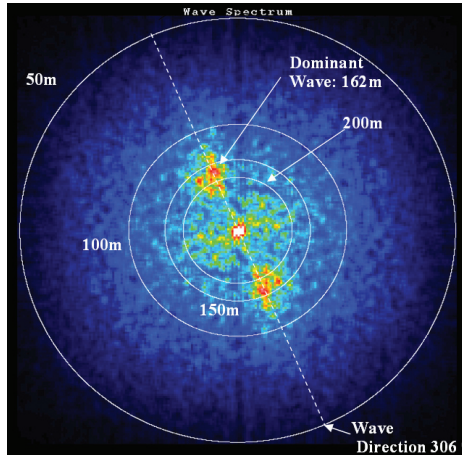
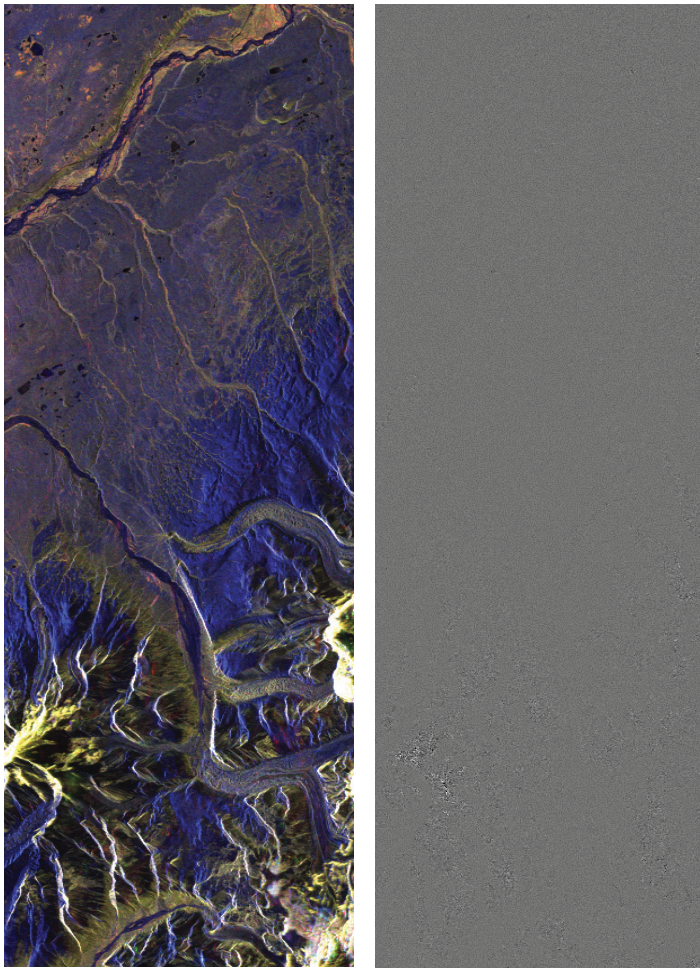


FIGURE 10.22 Spectrum of waves in the range direction using the alpha parameter from the Cloude Pottier decomposition method. Wave direction is 306° and dominant wavelength is 162 m.



(A) Pauli vector display

(B) Estimated Faraday rotation

FIGURE 10.23 Faraday rotation angle estimation from PALSAR PLR data of Gakona, Alaska: (A) The scene displayed with $|HH - VV|$ in red, $|HV| + |VH|$ in green, and $|HH + VV|$ in blue, and (B) Faraday rotation angles computed based on circular polarizations.

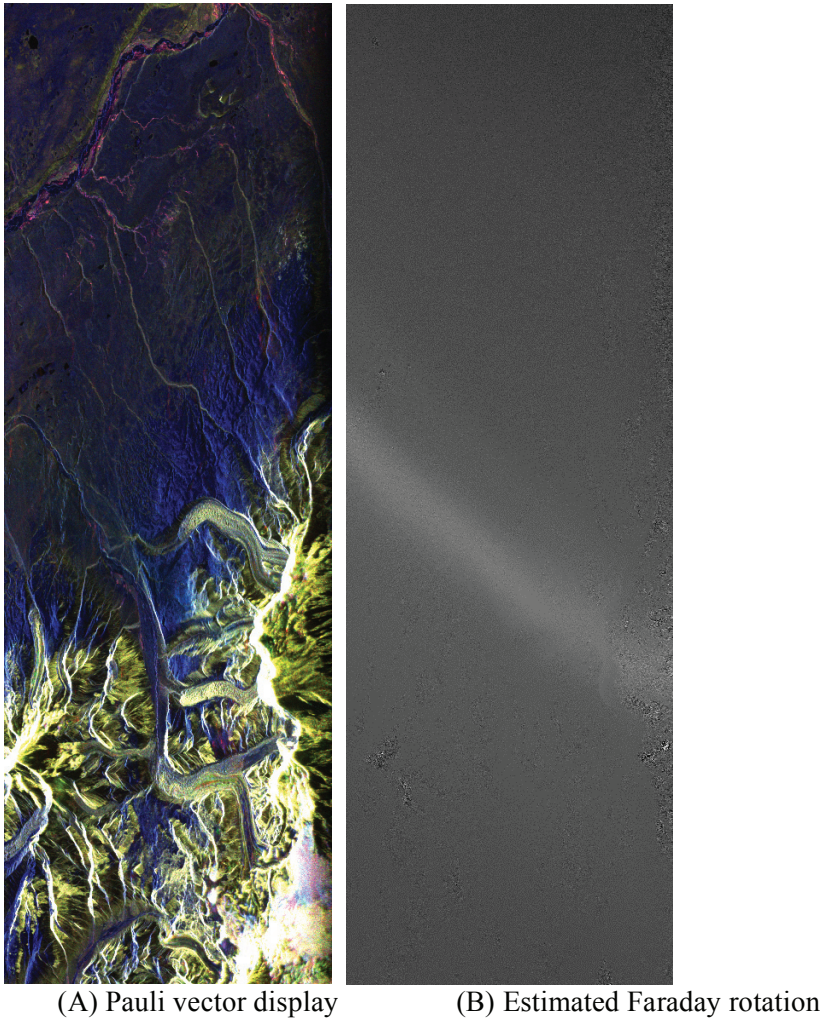


FIGURE 10.24 Faraday rotation angle estimation from ALOS PALSAR data of Gakona, Alaska, an interferometric pair of Figure 10.23: (A) The scene displayed with $|HH - VV|$ in red, $|HV| + |VH|$ in green, and $|HH + VV|$ in blue, and (B) Faraday rotation angles computed based on circular polarizations. Note that the bright feature in the center of the image, which could be the effect of an ionosphere irregularity.

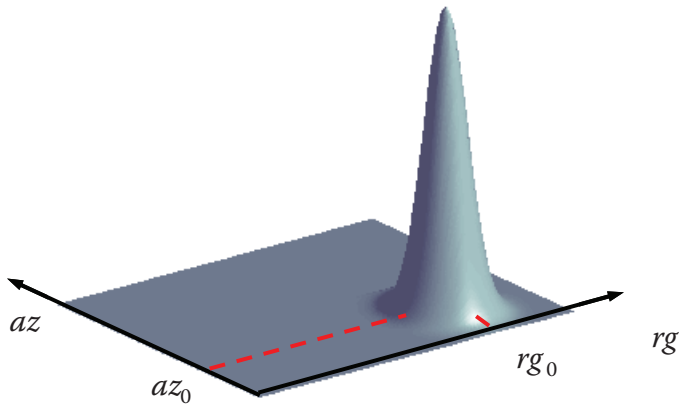


FIGURE 10.31 Example of an analyzing function for time-frequency analysis.

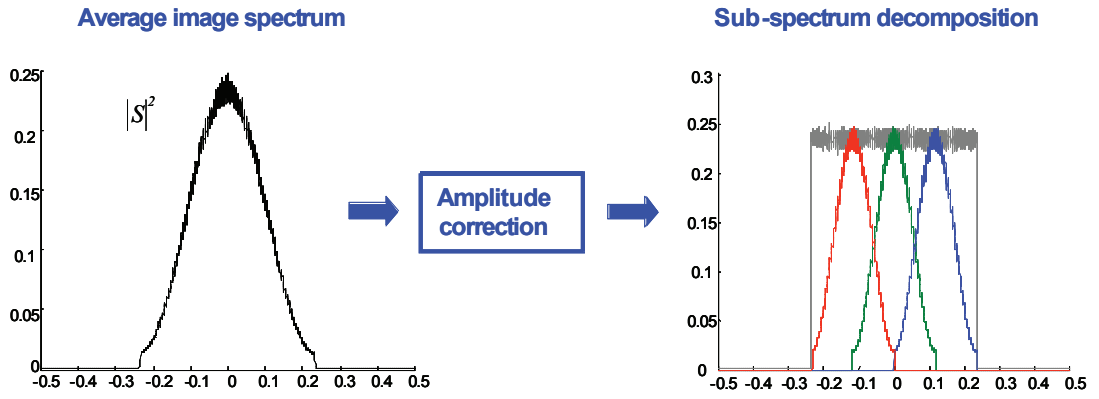


FIGURE 10.32 Estimation of the weighting function and spectrum decomposition in the azimuth direction.

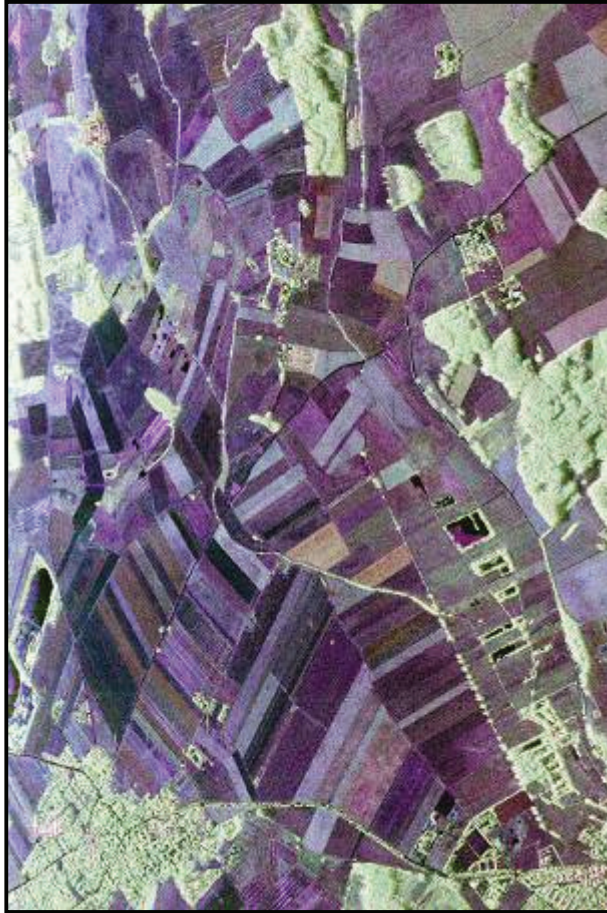


FIGURE 10.33 Polarimetric Pauli color-coded image of the Alling experiment area.

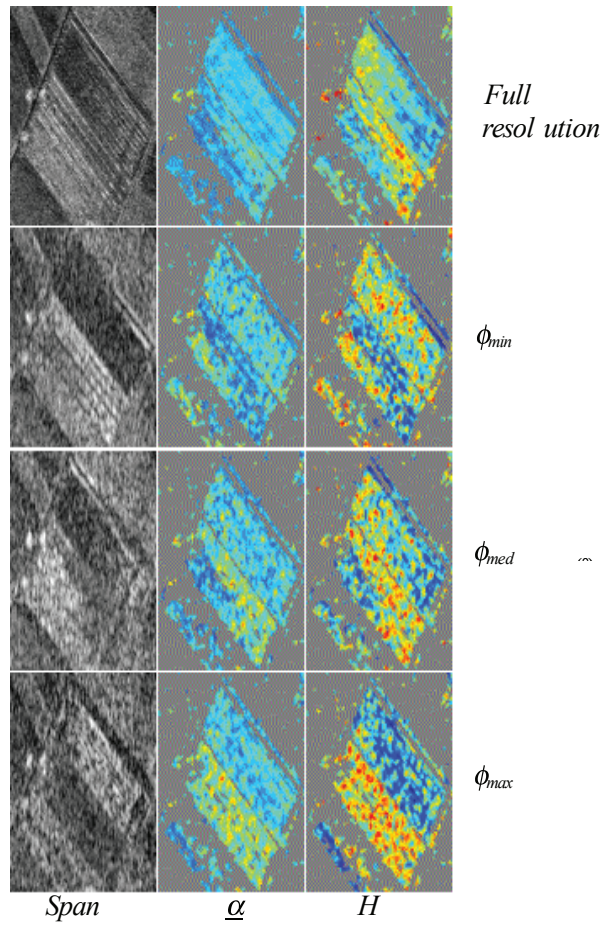


FIGURE 10.35 Polarimetric parameters over isolated fields at full resolution and after decomposition in the azimuth direction.

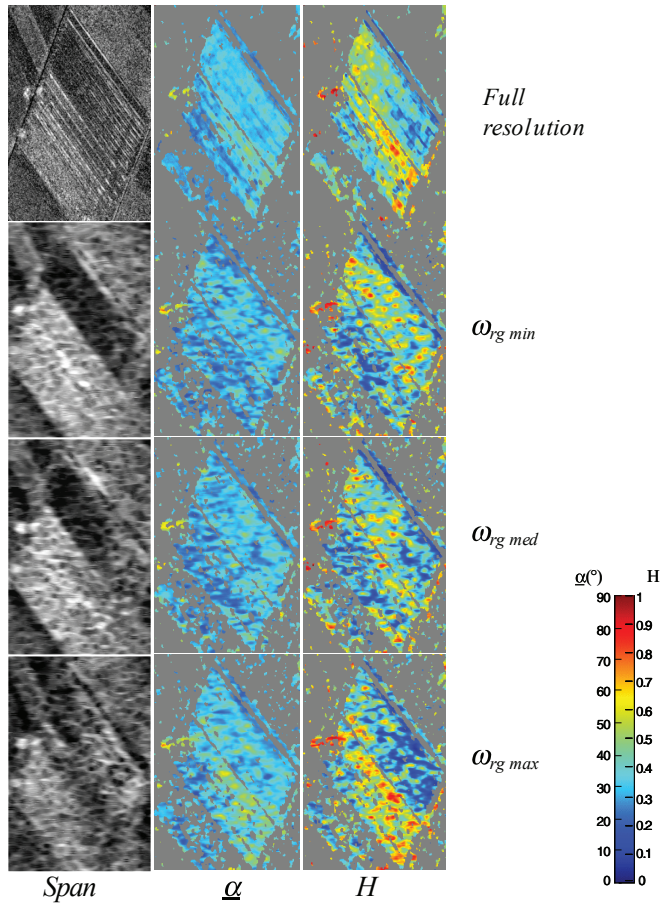


FIGURE 10.36 Polarimetric parameters over isolated fields at full resolution and after decomposition in the range direction.

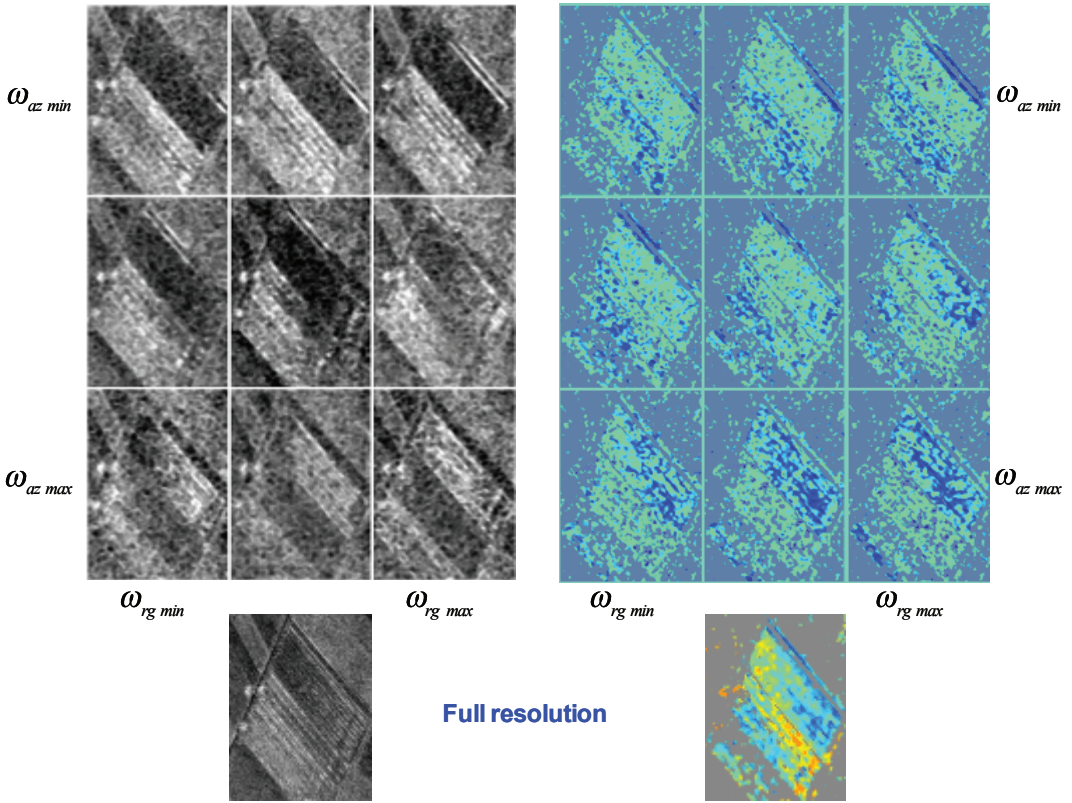


FIGURE 10.37 Polarimetric parameters over isolated fields at full resolution and after decomposition in range and azimuth directions.

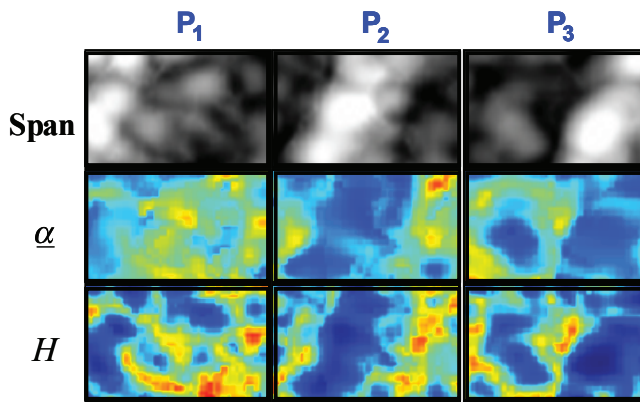


FIGURE 10.39 Representation of polarimetric characteristics in the range-azimuth frequency domain.

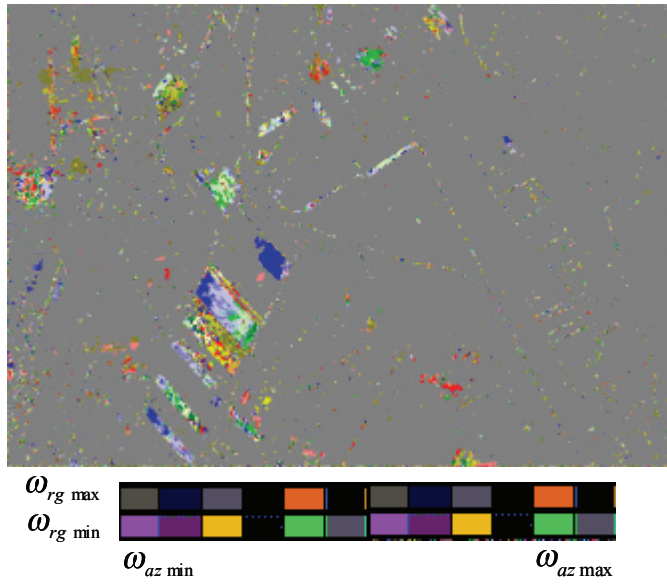
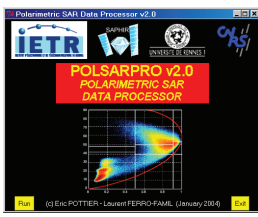


FIGURE 10.41 Location of the lowest probability subspectrum component among 12 range-azimuth subspectra for each nonstationary pixel.



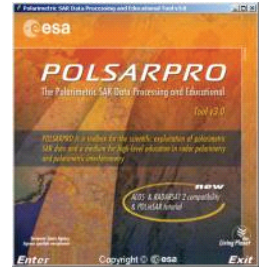
2003



2004



2005



2007

FIGURE B.1 PolSARpro main entry screen evolution.